

# A high-precision CO<sub>2</sub> densimeter for Raman spectroscopy using a Fluid Density Calibration Apparatus

Charlotte L. DeVitre<sup>a</sup>, Chelsea M. Allison<sup>a,b</sup>, Esteban Gazel<sup>a,\*</sup>

<sup>a</sup> Department of Earth and Atmospheric Sciences, Cornell University, Ithaca, NY 14850, USA

<sup>b</sup> The City College of New York, 160 Convent Avenue, New York, NY 10031, USA

## ARTICLE INFO

Editor: Catherine Chauvel

### Keywords:

Raman spectroscopy  
Carbon dioxide  
Fluid inclusions  
Melt inclusions  
Fluid Density Calibration

## ABSTRACT

Fluid and melt inclusions rich in CO<sub>2</sub> are common in many geological environments and are a powerful tool to provide constraints on P-T-X conditions of fluids resulting in ore deposits as well as pressures of inclusions in volcanic systems. Raman spectroscopy is an in situ, non-destructive method capable of determining the CO<sub>2</sub> densities of inclusions for most sample sizes (> 1 μm) and densities. However, significant discrepancies exist among published CO<sub>2</sub> densimeters for Raman spectroscopic measurements, mainly due to inconsistent calibration procedures, hardware differences, and sparse measurements for fluid densities between 0.2 and 0.7 g/mL. In this study, we re-designed a Fluid Density Calibration Apparatus (FDCA) based on one originally described by Lin et al. (2007) with important structural changes such as high accuracy temperature measurements made directly inside the FDCA that significantly reduce the error for critical region measurements. We provide five highly precise new calibration equations for different temperatures and CO<sub>2</sub> density ranges. Application of these equations to a set of melt inclusions from a Pico do Fogo eruption from Cabo Verde indicates that the total percent uncertainty in calculated CO<sub>2</sub> contents of bubbles derived from our densimeter are always below 5% except for inclusions with densities in the most sensitive part of the critical region (~7.3% for a 0.425 g/mL bubble), while relative percent uncertainty for literature densimeters are always above 10% and up to 28% in the worst-case scenario. In this study, we include all of the new designs, diagrams, and operational procedures with the goal of providing the community a new high-precision and high-accuracy FDCA for Raman spectroscopy.

## 1. Introduction

Carbon dioxide (CO<sub>2</sub>) is a volatile species important for life on Earth as well as for many geological processes. CO<sub>2</sub>-rich fluids are associated with many ore deposits of critical elements including gold, copper, and rare Earths (Baker, 2002; Fan et al., 2005; Groves et al., 2003; Lin et al., 2007; Roedder, 1979; Xie et al., 2009) and can also impact metamorphic and mantle processes (Ague, 2017; Andersen and Neumann, 2001; Dasgupta et al., 2004; Dasgupta and Hirschmann, 2010; Roedder, 1965). Additionally, CO<sub>2</sub> likely plays an important role in controlling volcanic explosivity (Allison et al., 2021; Roggensack et al., 1997). Fluid and melt inclusions, micron-sized fluids and melts captured during crystal growth, are the best way to determine the pre-eruptive volatile content of melts as their host can serve as a closed pressure vessel (Moore et al., 2015; Roedder, 1984; Steele-Macinnis et al., 2011 and references therein). Melt inclusions have therefore been at the forefront of studies seeking to constrain the record of pressure, temperature, and fluid

compositions (P-T-X histories) of geological processes (Roedder, 1984). Determining pressures of formation of host minerals (or entrapment pressures) from fluid and melt inclusions can be achieved by measuring the density of CO<sub>2</sub> contained in the inclusion and calculating CO<sub>2</sub> contents from mass balance (e.g., Esposito et al., 2012; Lamadrid et al., 2017; Moore et al., 2015; Roedder, 1965).

Raman spectroscopy is a non-destructive in situ method commonly used to measure the density of CO<sub>2</sub> in fluid and melt inclusions down to ~1 μm in size. Several studies have shown that the density of CO<sub>2</sub> can be calibrated as a function of the separation of the Fermi diad of CO<sub>2</sub> in the Raman spectrum (Fall et al., 2011; Kawakami et al., 2003; Lamadrid et al., 2017; Rosso and Bodnar, 1995; Song et al., 2009; Wang et al., 2011; Yamamoto and Kagi, 2006). CO<sub>2</sub> is a molecule with four vibrational modes, a symmetric stretching mode (ν<sub>1</sub>), an antisymmetric stretching mode (ν<sub>3</sub>), and two bending modes (ν<sub>2a</sub> and ν<sub>2b</sub>) (Rosso and Bodnar, 1995). ν<sub>1</sub> (1332.97 cm<sup>-1</sup>) is the only predicted Raman-active mode (Gordon and McCubbin, 1966) but because the ν<sub>1</sub> and second

\* Corresponding author.

E-mail address: [egazel@cornell.edu](mailto:egazel@cornell.edu) (E. Gazel).

<https://doi.org/10.1016/j.chemgeo.2021.120522>

Received 5 April 2021; Received in revised form 21 August 2021; Accepted 7 September 2021

Available online 9 September 2021

0009-2541/© 2021 The Authors.

Published by Elsevier B.V. This is an open access article under the CC BY-NC-ND license

(<http://creativecommons.org/licenses/by-nc-nd/4.0/>).

excited state of IR active  $\nu_2$  modes have nearly the same energy and the same symmetry species, they perturb each other in the excited states through a process known as Fermi resonance (Fermi, 1931). Both levels excite each other, admix, and the resonance causes them to split apart into two strong Raman bands instead of one. These two bands at roughly 1285.4 and 1388.2  $\text{cm}^{-1}$  are known as the Fermi diad (Fig. 1; Gordon and McCubbin, 1966; Rosso and Bodnar, 1995). Hot bands (Fig. 1) are the result of additional, higher vibrational states exciting and perturbing each other and splitting apart through Fermi resonance due to the thermal energy of the molecules with resultant Raman shifts of approximately 1264.8 and 1409.0  $\text{cm}^{-1}$  (Dickinson et al., 1929; Rosso and Bodnar, 1995). The weak band around 1370.0  $\text{cm}^{-1}$  in between the Fermi diad is due to isotopic splitting of  $^{13}\text{C}$ , typically present in less than 1% of molecules, and thus only apparent at relatively high densities of  $\text{CO}_2$  (Howard-Lock and Stoicheff, 1971; Rosso and Bodnar, 1995).

At low  $\text{CO}_2$  densities (<0.2 g/mL), all previously published densimeters (Fall et al., 2011; Kawakami et al., 2003; Lamadrid et al., 2017; Rosso and Bodnar, 1995; Song et al., 2009; Wang et al., 2011;

Yamamoto and Kagi, 2006) show a relatively linear relationship between Fermi diad separation and density (Lamadrid et al., 2017). This suggests that a densimeter can be calibrated for low  $\text{CO}_2$  densities using two or more  $\text{CO}_2$  standards (Lamadrid et al., 2017; Wieser et al., 2021). However, the existing densimeters also show large offsets from one another (e.g., Lamadrid et al., 2017), so they are not interchangeable. If these offsets are not corrected using  $\text{CO}_2$  standards, different densimeters can yield differences in  $\text{CO}_2$  densities on the order of  $\pm 0.1$  g/mL for a single Fermi diad separation, which propagate into variations in  $\text{CO}_2$  content of 1000s of ppm and depth uncertainties of several kilometers (Wang et al., 2011).

At densities >0.2 g/mL,  $\text{CO}_2$  densimeters are no longer linear and determination of  $\text{CO}_2$  density via Raman spectroscopy can be complicated as a result of the properties of the molecule. At room temperature ( $\sim 20^\circ\text{C}$ ) and  $\text{CO}_2$ -saturated conditions,  $\text{CO}_2$  densities between 0.2 and 0.7 g/mL (hereafter referred to as “mid-densities”) are not present as a single fluid phase but instead appear as co-existing low-density vapor and high-density liquid phases (V + L, Fig. 1b-c). To homogenize mid-density  $\text{CO}_2$  into a single phase, the temperature must be changed. Typically, this involves heating  $\text{CO}_2$  above its Critical temperature ( $T_c = 31.1^\circ\text{C}$ ; Fig. 1b-c) to homogenize into a single supercritical fluid phase.

Unfortunately, important discrepancies between densimeter equations exist at mid-densities (and higher). Some of these discrepancies might be explained by the fact that the existing densimeters contain only limited data at mid-densities, which in the critical region (near  $T_c$ ) can be prone to large amounts of uncertainty due to their sensitivity to small changes in temperature and pressure (Fig. 1c). Other possible sources for the discrepancies between densimeters include the experimental conditions and the analytical set-up of each laboratory (i.e., instrument type, laser wavelength, etc.). Finally, the environment (i.e., temperature) of each laboratory is subject to changes, which can lead to drift of the instrument that may require frequent calibration to guarantee the accuracy of measurements. This mid-density region can be quite important for natural samples, in particular for melt inclusion bubbles. While many melt inclusion bubbles do have fairly low densities (i.e., <0.2 g/mL vapor), some samples do fall into this mid-density region (e.g., Moore et al., 2015; Aster et al., 2016). Microthermometric analysis can be quite difficult or impossible for these samples (e.g., Rosso and Bodnar, 1995) depending on the density of  $\text{CO}_2$ , the size of the bubble, and overall optical clarity so they require Raman spectroscopic analysis and accurate  $\text{CO}_2$  densimeters.

Previous  $\text{CO}_2$  densimeters for Raman spectroscopy were calibrated using a variety of techniques, including multiple styles of fluid density calibration apparatus (FDCA) (e.g., Fall et al., 2011; Lamadrid et al., 2017; Wang et al., 2011). However, the use of FDCA devices to calibrate Raman  $\text{CO}_2$  densimeters is not currently standard practice, possibly because the published schematics and operating procedures of existing FDCA devices are not detailed enough for easy reproduction. Careful calibration of a Raman instrument is critical for any laboratory seeking to understand geological processes through fluid and melt inclusion studies. Therefore, it is essential that the design and operation of FDCA devices is accessible in the literature.

In this study, we present a redesigned FDCA (after Fall et al., 2011; Lamadrid et al., 2017; Lin et al., 2007) with important structural modifications to increase the precision and accuracy of the density measurements, particularly in the critical region of  $\text{CO}_2$ . We make the designs and diagrams available and describe our method with detail in the hope that this will make the process of building such calibrations routine work in other laboratories working with fluid and melt inclusions to elucidate Earth processes. Finally, we demonstrate the potential pitfalls of applying an externally calibrated Raman  $\text{CO}_2$  densimeter, and the necessity of internal calibration.

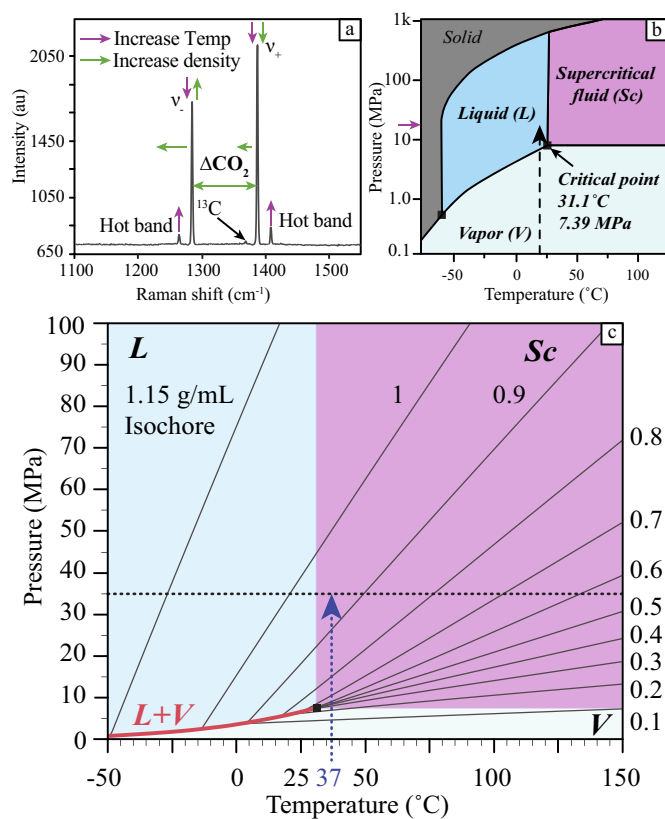


**Fig. 1.**  $\text{CO}_2$  and Raman spectroscopic data. a) Representative Raman spectrum of  $\text{CO}_2$  showing the Fermi diad, hot bands and the effects of increasing temperature and density on the position and intensity of the Raman bands.  $\Delta\text{CO}_2$  is the separation (split) of the Fermi diad: it is calculated as the difference between the peak position of the upper band  $\nu_+$  and lower band  $\nu_-$ . Intensity is shown in arbitrary units. Modified from Rosso and Bodnar (1995) with our own Raman data. b) Phase diagram of  $\text{CO}_2$ . The dashed arrow represents the path of  $\text{CO}_2$  at constant room temperature. The solid arrow is the maximum pressure reached during our experiments. c) Closeup of the phase diagram of  $\text{CO}_2$ . The black lines are isochores drawn for densities between 1.15 g/mL and 0.1 g/mL calculated using the EOS of Span and Wagner (1996). The red line is the liquid+vapor curve, which represents the range of pressures and temperatures at which liquid and vapor  $\text{CO}_2$  coexist. The black dashed line is the maximum pressure of our experiments and the blue dashed arrow indicates the supercritical temperature of our experiments. (For interpretation of the references to colour in this figure legend, the reader is referred to the web version of this article.)

## 2. Experimental setup

### 2.1. Fluid Density Calibration Apparatus (FDCA) design

The separation of the Fermi diad of CO<sub>2</sub> ( $\Delta$ CO<sub>2</sub>) on a Raman spectrum is correlated with the density of CO<sub>2</sub> (e.g., Rosso and Bodnar, 1995), which is a function of pressure and temperature related by an Equation of State (EOS; e.g., Span and Wagner, 1996). We calibrate the CO<sub>2</sub> density from Raman spectra using a redesigned FDCA. Different kinds of apparatuses have been used as FDCAs in the literature to determine the PT dependence of methane stretching bands (Lin et al., 2007) as well as the density of CO<sub>2</sub> (Fall et al., 2011; Garrabos et al., 1989a, 1989b, 1980; Kawakami et al., 2003; Lamadrid et al., 2017; Rosso and Bodnar, 1995; Song et al., 2009; Wang et al., 2011; Yamamoto and Kagi, 2006). Our modified experimental setup is similar to the FDCA from Lin et al. (2007), Fall et al. (2011), and Lamadrid et al. (2017) in

that the density of CO<sub>2</sub> is determined from the pressure and temperature inside a small chamber of CO<sub>2</sub>.

The system consists of 12 main components (Fig. 2, parts labeled 1–12) acquired primarily from High Pressure Equipment Co. (HiP) (see Supplemental materials S2 and S5 for details and photographs for all parts). Overall, this FDCA consists of four main sections separated by on/off valves. The first section consists of a cylinder of research grade (99.999% purity) CO<sub>2</sub> (part labeled 1.a in Fig. 2: Size 200 cylinder, CGA-320 connection, AIRGAS part #CD-R200) that is connected to the system via 1/16" capillary stainless-steel tubing and a 1/4" HF4 ON/OFF valve (part labeled 2 in Fig. 2: Valve A, HiP part #60-11HF4). For safety, we attached a 1/4" NPT Check Valve (part labeled 1.b in Fig. 2: HiP part #15-41NFB) to the cylinder (via a CGA-320 to 1/4" NPT Nut & Nipple fitting) to prevent any back flow into the cylinder during pressurization of the system. The 1/16" OD stainless steel tubing (HiP part #15-9A1-006) was used for mobility purposes. The connections to the 1/16"

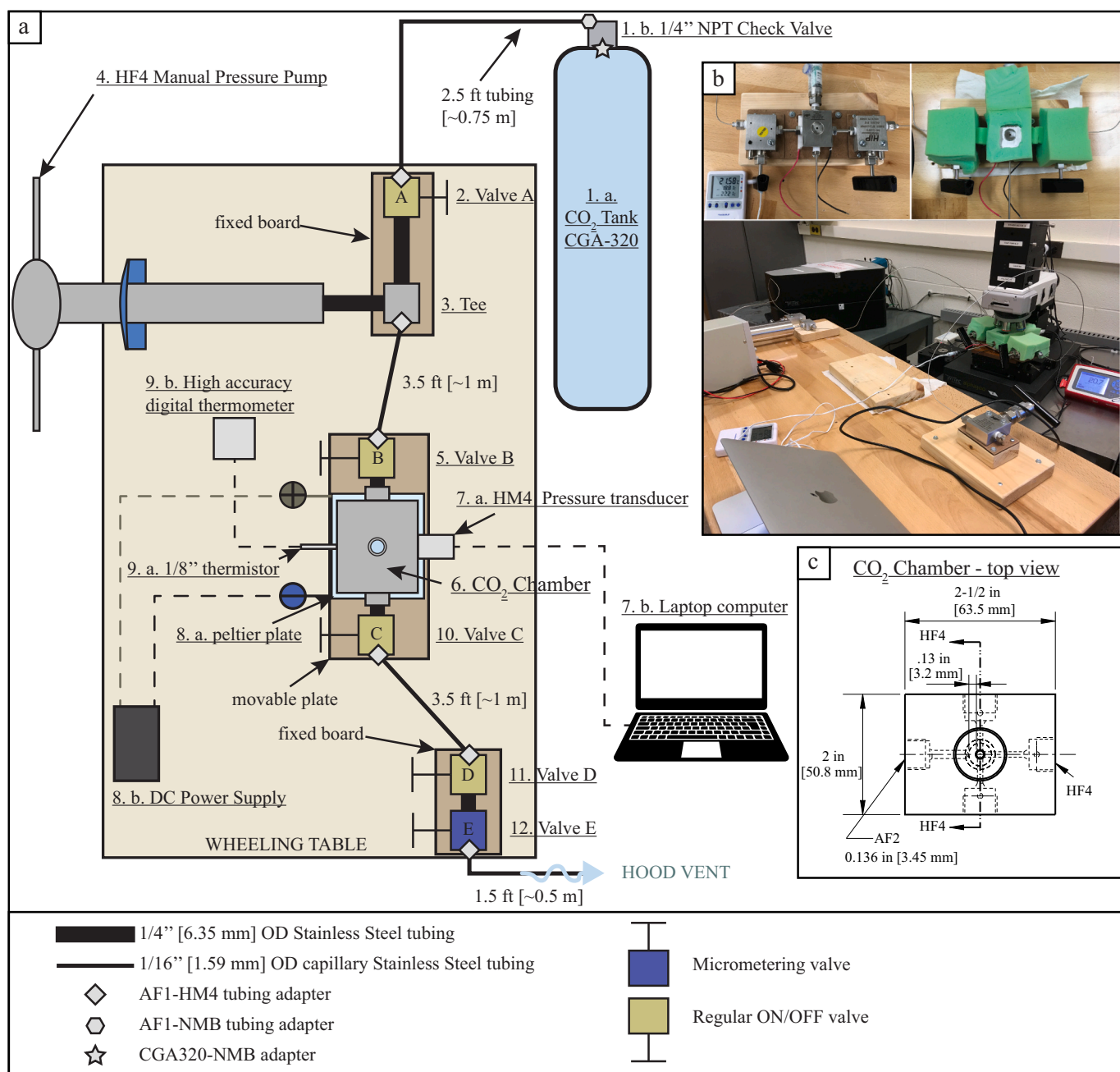


Fig. 2. Detailed diagram of the Fluid Density Calibration Apparatus (FDCA) including design of the FDCA's central component.

tubing require an AF1-NMB adapter (HiP part #15-21AF1NMB) on the check valve and an AF1-HM4 adapter (HiP part #15-21AF1HM4) on the ON/OFF valve.

The second section of the FDCA sits between ON/OFF valves A and B and is where pressurization of CO<sub>2</sub> takes place. Valve A is connected to a high-pressure tee (part labeled 3 in Fig. 2; HiP part #60-23HF4) via 1/4" high-pressure coned and threaded tubing (HiP part #60-HM4-2.75), which is in turn connected to a 20-cc manual pressure pump generator (HiP part #50-6-15). The pressure pump generator is fixed directly to the table with hex bolts while valve A and the high-pressure tee are leveled on a wooden plank which is fixed to the table with self-screwing hex screws. The third end of the high-pressure tee (part labeled 3 in Fig. 2) is connected to another ON/OFF valve (part labeled 5 in Fig. 2) via 3.5 ft. of the 1/16" OD stainless steel tubing. Again, the 1/16" tubing requires AF1-HM4 adapters to attach to the HF4 connections of the tee and valve.

The third section of the FDCA contains the CO<sub>2</sub> chamber between ON/OFF valves B and C. Valve B is connected to the CO<sub>2</sub> chamber (part labeled 6 in Fig. 2) via 1/4" high-pressure coned and threaded tubing (HiP part #60-HM4-2.75). The CO<sub>2</sub> chamber (Fig. 2, bottom right panel) is a custom-designed high-pressure cross from HiP rated at 5000 psi (34.47 MPa) at 100 °F (37.78 °C). The CO<sub>2</sub> chamber has three high pressure connections (HF4), one medium pressure (AF2) connection for a thermal probe and a fused-quartz window at the top (3.2 mm diameter opening). Pressure is recorded in real-time on a laptop computer at 1 Hz frequency and measured directly inside the CO<sub>2</sub> chamber using an HM4 connection ESI USB pressure transducer (part labeled 7a in Fig. 2; Genspec Dynamic GD4200-USB, 0–1000 bar) with 0.15% accuracy of the best-fit standard line. Temperature is also measured directly inside the CO<sub>2</sub> chamber using a Digi-Sense 90,000–29 steel probe extreme accuracy thermometer (parts labeled 9a-b in Fig. 2) with a resolution of 0.01 °C and an accuracy of ±0.05 °C from –2 to 2 °C, 23 to 27 °C, and 35 to 39 °C. The CO<sub>2</sub> chamber sits on a square Thermoelectric “Peltier” Plate (from TE Tech, see S2) of 42 mm thickness connected to a Tekpower TP3005N Regulated DC Power Supply (0–30 V at 0–5 A; acquired on Amazon.com, see S2) to provide a stable and adjustable temperature during the experiment. The CO<sub>2</sub> chamber is connected to another ON/OFF valve (valve C, part labeled 10 in Fig. 2) through 1/4" high-pressure coned and threaded tubing (HiP part #60-HM4-2.75). Valves B, C, and the CO<sub>2</sub> chamber are fixed to a thin (3/16") but rigid 10" x 3" hardboard to facilitate placement on the Raman instrument and prevent accidental torque on components when moving this section of the FDCA. We selected thin hardboard for this purpose because the maximum allowable working distance of the WITec Alpha 300R Raman instrument used in this study is 5.5 cm. The working distance of other instruments may vary, and adjustments should be made accordingly. An additional piece of hardboard of equivalent thickness to the Peltier Plate is placed under valves B and C to ensure that all connections are tight and level.

The final section is after valve C and is where CO<sub>2</sub> is removed from the system. Valve C is connected to a micro control metering valve (valve E, part labeled 11 in Fig. 2; HiP part #60-11HF4-V) which allows for precise and slow release of pressure from the system. The micro control valve is designed to be paired with an additional ON/OFF valve (valve D, part labeled 11 in Fig. 2) to avoid damage to the highly sensitive micro control valve so that it can be kept open at the desired flow rate. Due to design changes during testing of this setup, we substituted a pressure plug at the end of the micro-control valve (E) instead of using valve D to protect the system from damage. However, we prefer the use of the additional ON/OFF valve (valve D) rather than the pressure plug method. The final valve E is connected to 1/16" tubing that vents into a fume hood.

The entire FDCA system sits on a sturdy hardwood table with locking wheels for mobility. A thick, soft foam block was carved to fit the setup and insulate the system to maintain constant temperature while the experiment is running.

## 2.2. Critical components of an FDCA system for high accuracy and ease of use

One of the most critical components of the redesigned FDCA is to measure both temperature and pressure directly inside the CO<sub>2</sub> chamber. This is because Raman CO<sub>2</sub> densimeters are calibrated by measuring  $\Delta$ CO<sub>2</sub> as a function of temperature and/or pressure, which is converted to CO<sub>2</sub> density using an EOS, such as that of Duschek et al. (1990), Sterner and Pitzer (1994), or Span and Wagner (1996). Previous studies have suggested that the differences in CO<sub>2</sub> density resulting from choice of EOS are fairly small and cannot explain the differences between densimeters (Lamadrid et al., 2017). We selected the EOS from Span and Wagner (1996), available as an online NIST calculator (<http://webbook.nist.gov/chemistry/fluid/>) due to the ease of use and because it has been used in other CO<sub>2</sub> densimeters (Fall et al., 2011; Lamadrid et al., 2017; Song et al., 2009; Wang et al., 2011).

Calibration of mid-density (~0.2–0.7 g/mL) data in particular is greatly improved by measuring temperature and pressure directly within the CO<sub>2</sub> chamber. In the critical region, every EOS is highly sensitive to differences in temperature and pressure (calculated at 37 °C in Fig. 3a-b) for mid-densities (~0.2–0.7 g/mL). At higher temperatures, the density is much less sensitive to small changes in pressure and temperature, but to calibrate a full range of densities from 0.01 to 1 g/mL at a constant high temperature requires a very large pressure range (e.g., 0–100 MPa at 90 °C; Fig. 1c). We therefore chose to run our calibrations with a supercritical temperature of 37 °C since it maximizes the range of densities covered by our densimeter in a short pressure interval (0–35 MPa) while still permitting high precision in the critical region. Our thermistor probe is calibrated for high accuracy (<0.05 °C) within 2 °C of 3 points (0, 25, and 37 °C) to ensure that we attain the maximum temperature accuracy for both our room temperature and supercritical temperature calibrations.

We note that it is also possible to calibrate some mid-density data at temperatures lower than T<sub>C</sub>, although we did not pursue this in our study. The temperature at which the L + V phases homogenize into a single phase is a function of the density of CO<sub>2</sub> (Fig. 1c). For CO<sub>2</sub> with densities between ~0.6 and 1 g/mL, L + V homogenizes to pure liquid at temperatures from –14 to ~29 °C and becomes a supercritical fluid at temperatures ≥T<sub>C</sub>. For CO<sub>2</sub> densities between 0.4 and 0.6 g/mL, pure liquid is never reached and L + V changes to a supercritical fluid at ~T<sub>C</sub>. Finally, for densities below ~0.4 g/mL, pure liquid is never attained and instead, L + V homogenizes to vapor CO<sub>2</sub> between 30 and –56 °C and changes into a supercritical phase when critical pressure is reached (7.39 MPa, Fig. 1b-c). This means that at temperatures ≥T<sub>C</sub>, CO<sub>2</sub> measured will always be a single homogeneous vapor or supercritical phase (depending on the density of CO<sub>2</sub>), which is why we designed the FDCA specifically for measurements at room temperature or temperatures ≥T<sub>C</sub>.

The EOS is also highly sensitive to changes in pressure, where an uncertainty of ±0.05 MPa in the critical region can cause up to ±0.05 g/mL uncertainty on the density (Fig. 3a). For pure liquid (i.e., 0.9 g/mL) or vapor (i.e., 0.1 g/mL) densities, an uncertainty of ±0.05 g/mL correlates with ~19 MPa and ~4 MPa difference in pressure, respectively (Fig. 3b). These represent relative errors in pressure of ~65% at high density (CO<sub>2</sub> liquid) and ~70% at low density (CO<sub>2</sub> vapor), but less than 4% in the highly sensitive critical region of CO<sub>2</sub>. For this reason, it is important to measure pressure with high accuracy (better than 0.15% of pressure output), directly connected to the CO<sub>2</sub> chamber component (part labeled 7a in Fig. 2). Previous densimeters have used high-accuracy pressure gauges (i.e., 0.10% and 0.25% of the pressure output in Lamadrid et al., 2017) and in the case of our experiments, the maximum uncertainty in pressure was ~0.05 MPa at the highest pressure, ~0.01 MPa in the critical region and ~0.0001 MPa at the lowest pressure. The uncertainty in pressure translates to negligible errors in the density (<0.0001 g/mL) at the high and low ends of the region of interest and <0.01 g/mL error at the most sensitive part of the critical region (Fig. 3a).

Temperature uncertainties can also have a serious impact on the



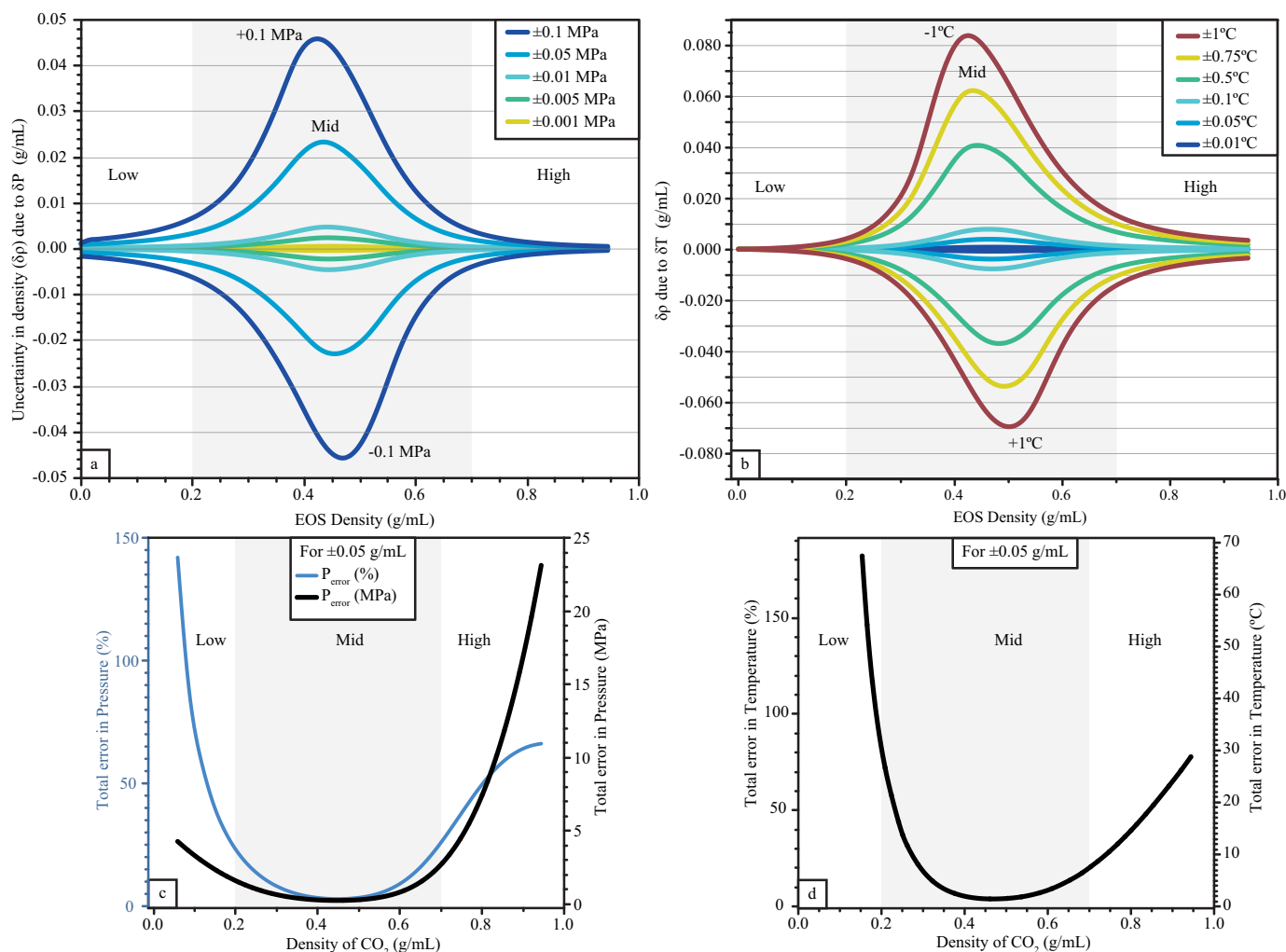


**Fig. 3.** Uncertainties in  $\text{CO}_2$  density calculated through the Span and Wagner (1996) as a result of uncertainties in pressure (a) and temperature (c). Calculations were done using  $37^\circ\text{C}$  to show the critical region of  $\text{CO}_2$  densities. a) Uncertainty in density caused by varying degrees of uncertainty in pressure measurements. b) Uncertainty in density caused by varying degrees of uncertainty in temperature measurements. c) Total error in pressure needed to produce  $\pm 0.05$  g/mL error in the density. d) Total error in temperature needed to produce  $\pm 0.05$  g/mL error in the density. The curves for total % error and the total  $^\circ\text{C}$  error in temperature overlap each other. Shaded regions show mid-densities which require homogenization into a supercritical phase to be measured - otherwise two phases with two separate densities (Liquid and Vapor) are present. Regions are labeled low-density (Low), mid-density (Mid) and high-density (High).

quality of the data, particularly in the critical region (Fig. 3c). At mid-densities (i.e.,  $37^\circ\text{C}$  and 8–9 MPa) a temperature uncertainty of  $\pm 0.6^\circ\text{C}$  yields an uncertainty of  $\pm 0.05$  g/mL in the density as calculated by the EOS. At pure liquid (i.e., 0.9 g/mL) or vapor (i.e., 0.1 g/mL) densities, an uncertainty of  $\pm 0.05$  g/mL correlates with temperature differences of  $\sim 30^\circ\text{C}$  and  $\sim 70^\circ\text{C}$ , respectively (Fig. 3d). These represent relative errors in temperature of  $\sim 78\%$  at high density and  $\sim 180\%$  at low density but less than 4% in the most sensitive part of the critical region of  $\text{CO}_2$ . Typical thermocouples that were used for some of the published densimeters have accuracies between  $\pm 1^\circ\text{C}$  (for types E, J, K) and  $\pm 2^\circ\text{C}$  (for type N). Even if the variation in temperature is kept within  $0.05^\circ\text{C}$  during acquisition, such uncertainty could cause enormous amounts of error in density in the critical region ( $\pm 0.08$  g/mL).

An additional source of uncertainty in the temperature could result from not measuring the temperature of  $\text{CO}_2$  directly inside the  $\text{CO}_2$  chamber but rather measuring the temperature near the chamber within the steel wall (i.e., Fall et al., 2011; Lamadrid et al., 2017). Steel is a poor thermal conductor ( $16\text{ W m}^{-1}\text{ K}^{-1}$  for 316 stainless steel) compared to other metals, but similar in order of magnitude to that of single-crystal olivine ( $\sim 1\text{--}10\text{ W m}^{-1}\text{ K}^{-1}$  at room temperature and 1 atm) depending on forsterite content, structure, water in the lattice, pressure, and

temperature (Xiong and Zhang, 2019; Chang et al., 2017). However, its conductivity is 10 to 100 times higher than that of pure  $\text{CO}_2$  depending on the phase it is in (e.g.,  $\sim 0.18\text{--}0.11\text{ W m}^{-1}\text{ K}^{-1}$  for liquid and  $\sim 0.08\text{--}0.03\text{ W m}^{-1}\text{ K}^{-1}$  for vapor also depending slightly on temperature and density). Hence the temperature of the steel wall may significantly differ from the temperature of the  $\text{CO}_2$  fluid. Additionally, heat radiation or conduction from the steel walls to the environment could also cause significant differences in the temperature of the container and the fluid. We compared the temperature of the steel pressure sensor with the internal temperature of the fluid, which showed that the temperature of the pressure sensor was  $\sim 32^\circ\text{C}$  while the fluid inside the cell was stable at  $37^\circ\text{C}$ . This test indicates that measurements of temperature outside of the  $\text{CO}_2$  chamber could misrepresent the fluid temperature and introduce additional uncertainty. For this reason, it is of utmost importance to select a probe and thermometer with high accuracy, preferably a thermistor with high accuracy ( $<0.05^\circ\text{C}$ ), but also to measure the temperature directly inside the cell apparatus rather than on the steel wall.

One additional component that we found critical for the redesigned FDCA was a foam insulation cover placed on the central block (parts labeled 5–10 in Fig. 2) to maintain stable temperature of the system. The

foam block contains an opening over the quartz window to allow for Raman analyses. An anti-freeze or water bath can also be used to stabilize the temperature but may prove to be challenging given the design of the FDCA. An insulating cover provides a sufficient barrier to thermal diffusion in the system to ensure high temperature stability ( $<0.01$  °C variation of the temperature during acquisition).

The central block of the FDCA (containing the CO<sub>2</sub> chamber; parts 5–10 in Fig. 2) is attached to a moveable block to ensure that it can easily be placed under the Raman microscope. To achieve this mobility, the block is connected to the rest of the system via small diameter (1/16") flexible steel tubing.

Another critical component of the FDCA is that the section between valves A and B where pressurization takes place should be built with as small of a volume as possible (excluding the volume of the pressure pump itself). This will ensure that pressurization up to 34 MPa requires no more than 2 full strokes of the pressure pump. The remaining volume of the FDCA should also be built with a small volume so that equilibration in P and T can be efficient ( $<5$  min) between each step.

Finally, we use a thermoelectric "Peltier" plate to provide high precision temperature control on the FDCA. This allows for excellent and stable temperature control during the experiment and during acquisition and is preferred over a typical hot plate because temperature adjustments can be made within seconds.

### 2.3. FDCA system operation

The FDCA was designed to be used over long periods of time (12+ hours) so that calibrations can be run continuously as needed. Before starting any calibration experiment, it is imperative to check for leaks in the FDCA system (see Supplementary materials S6 for short videos). The easiest way to do this is by closing the exit valve (D) and submerging the central portion of the setup (Valves B, C and the CO<sub>2</sub> chamber) under water in a large, wide plastic container. If there is evidence for multiple leaks, the test can be done connection by connection by simply using plugs on all but the input line and successively adding components after no leakage has been confirmed. Before submerging the CO<sub>2</sub> chamber, the Peltier stage should be removed, as it is not waterproof. The plate on which the chamber is sitting can be submerged but if hardboard or wood was used instead of metal it is still preferable to remove it to avoid water damage from multiple leak tests over time. Prior to submerging, it is useful to use paraffin paper to seal the cabled ends of the pressure transducer and thermistor probe to avoid water infiltration. Additionally, it is best to keep the cables at the end of the transducer and thermistor upward and to not submerge the setup more than is needed to have a thin layer of water above the window. Upon opening the CO<sub>2</sub> cylinder valve and carefully inspecting the setup, bubbling of any connections will immediately reveal system failures. It is worthwhile to note that failures will be more evident at higher pressures ( $> 6$  MPa), so it is useful to perform this test at higher pressures and monitor the pressure for stability throughout the experiment. If any leaking is observed, undoing and cleaning the connections with compressed air followed by re-taping and careful re-assembling should fix any issues. Once the FDCA is stable, the operational procedure for the experiment is as follows:

- 1) Start the pressure recording software and leave the FDCA to equilibrate at atmospheric pressure (all ON/OFF valves open; CO<sub>2</sub> cylinder should remain closed) for at least 40 min in the room where the experiment will be conducted. Once the pressure and temperature curves of the sensor have stabilized, the sensor can be zeroed, and the recording will restart. This step ensures that the pressure recording is as accurate as possible.
- 2) With all ON/OFF valves open, next open the cylinder of research grade purity (99.999%) CO<sub>2</sub> and purge the FDCA continuously for 2 min. This will remove any other gases and/or water from the line. The outlet of the system should be placed in a fume hood during this purge. Before starting the purge, the manual pressure pump's wheel should be turned all the way in (smallest volume). After 2 min, close valve D and allow the pressure inside the cell to equilibrate with the cylinder pressure (at least 3–5 min) and the sensor's temperature should equilibrate as well.
- 3) Turn on the Peltier plate to heat the CO<sub>2</sub> chamber. The voltage required will depend on the Peltier plate, DC power supply and the desired temperature as well as the pressure of the system (voltage may need to be adjusted during the experiment to ensure the temperature remains stable). In the case of our setup, a 1.7 V supply at the pressure of the CO<sub>2</sub> cylinder was found to provide a stable temperature of 37 °C. When running a calibration at 37 °C, we initially heat the CO<sub>2</sub> chamber using  $\sim 2$ –3 V to reach the desired temperature more rapidly. Once a temperature of  $\sim 34$  °C has been reached we lower the voltage to 1.7 V and leave the CO<sub>2</sub> chamber to stabilize for  $\sim 10$ –20 min. We find that it should not be necessary to close off the CO<sub>2</sub> chamber at this step. To avoid over-pressurizing the system, heat the CO<sub>2</sub> chamber to 37 °C before pressurizing beyond the pressure of the CO<sub>2</sub> cylinder. Because "room temperature" is highly variably depending on the room, season, time of day, etc., we recommend using the Peltier stage even for room temperature measurements. We keep the CO<sub>2</sub> chamber at a temperature of about 24 °C since the thermometer is accurate to  $\pm 0.05$  °C within 2 °C of 0 °C, 25 °C and 37 °C. For our setup, a 0.09 V supply was sufficient at the pressure of the CO<sub>2</sub> cylinder to keep the temperature stable.
- 4) Once the desired temperature has been reached, start the pressurization process. First, make sure all valves except D are open (Fig. 2). Next, turn the manual pressure pump's wheel all the way out (maximum volume) to draw CO<sub>2</sub> from the cylinder into this newly available volume. Then, close valve A and turn the wheel in to the minimum volume (the piston will raise the pressure in the system due to the decrease in volume). If the desired pressure is not reached at this step, draw more CO<sub>2</sub> into the system. Start by closing valve B then open valve A and turn the wheel to maximum volume to draw more CO<sub>2</sub> into the system. Next, close valve A, open valve B, and turn the wheel all the way to minimum volume (or stop turning the wheel once the desired pressure is reached). Once the maximum desired pressure is reached, valve A will remain closed. If this FDCA is reproduced exactly, two cycles of opening/closing the pressure wheel will be sufficient to reach 34 MPa. Should the system fail to reach pressure, the connections should be checked for leakage.
- 5) Once pressure is reached, leave the CO<sub>2</sub> chamber to re-equilibrate its temperature and pressure ( $\sim 10$ –20 min). Additionally, make sure the insulation foam cover is placed on the setup at this time to ensure successful equilibration and stability of the temperature inside the CO<sub>2</sub> chamber. The voltage of the Peltier plate will likely need to be increased (up to 1.9–2.0 V at high T or 1.0–1.2 V at room T) to maintain the temperature of 37 °C or 24 °C. It is important to note that the temperature of the pressure sensor must also equilibrate to ensure the pressure readings are as precise as possible. While waiting for the system to equilibrate, place the block containing valves B, C, and the CO<sub>2</sub> chamber on the stage of the Raman instrument and focus inside the CO<sub>2</sub> chamber to prepare for analysis.
- 6) Once the system has equilibrated, close valves B and C and allow the CO<sub>2</sub> chamber pressure to equilibrate ( $\sim 2$ –3 min). In response to the volume decrease, the pressure will increase  $\sim 0.02$  MPa upon closure of the valves, so the pressures targeted need to account for this change. We recommend performing a double equilibration (steps 5 and 6) as it reduces the overall disequilibrium in the system which facilitates adjustments before the next data point is acquired.

- 7) To accommodate for laser heating ( $+0.02\text{ }^{\circ}\text{C}$ ), the temperature of the FDCA should be left to equilibrate for about 2–3 min with the laser on prior to acquisition.
- 8) To reduce the pressure inside the  $\text{CO}_2$  chamber to obtain a full spectrum of  $\text{CO}_2$  density analyses, turn the wheel of the manual pressure out (increase the volume) in small steps as needed. To do this, open valves B and C after an acquisition and turn the wheel out until the new desired pressure is reached. Close valves B and C and allow  $\sim 3$  min for the  $\text{CO}_2$  chamber to re-equilibrate.
- 9) At some point during these incremental pressure decreases, the pressure wheel will reach its minimum volume. To reduce the pressure further,  $\text{CO}_2$  must be bled from the system. To do this, first ensure that the pressure wheel is turned all the way back in so that  $\text{CO}_2$  is bled at the minimum volume of the system (this will allow use of the pressure wheel to reduce pressure in small steps). Next, open valves B and C, then carefully open and close valve D until the desired pressure is reached (considering the 0.02 MPa increase due to volume reduction upon closing valves B and C). The new pressure should equal the minimum pressure reached in the previous acquisition. After bleeding  $\text{CO}_2$  from the system, re-equilibration of the temperature may take 5–10 min.
- 10) Repeat steps 6 through 9 until the calibration is completed. Note that the minimum pressure the system can be safely bled to is  $\sim 0.17$  MPa to ensure no atmospheric contamination occurs. By turning the pressure wheel out to maximum capacity, the minimum pressure that can be reached starting from 0.017 MPa is  $\sim 0.035$  MPa.

### 3. Constructing a new high-precision Raman $\text{CO}_2$ densimeter

#### 3.1. Analytical conditions

Spectra were collected using a WiTec Alpha 300R Raman spectrometer at the Cornell Center for Materials Research equipped with a UHTS 600 VIS spectrometer (600 mm focal length), a back-illuminated CCD camera with  $1024 \times 127$  pixel format ( $26 \times 26$   $\mu\text{m}$  size) and a 531.885 nm (green) laser focused with a  $5\times$  objective ( $\times 0.25\text{NA}$ , 25 mm focal distance). Given their small size, measurements of fluid and melt inclusions are usually done using  $20\times$ ,  $50\times$  or  $100\times$  objectives to maximize confocality and resolution. However, the use of different microscope objectives does not significantly affect the position of the peaks or the separation of the Fermi diad of  $\text{CO}_2$  (Lamadrid et al., 2017). For instance, we found a non-significant 0.002 g/mL difference between densities calculated from data acquired using  $20\times$  and  $50\times$  objectives on fused silica capillary  $\text{CO}_2$  standards. However, the objective selection does bear significance to the intensity of the signal (lower magnification objectives provide stronger signal because they analyze larger volumes) and can facilitate more precise peak fitting (Lamadrid et al., 2017). Therefore, a  $5\times$  objective was selected to maximize the volume reached in the FDCA.

Each analysis from August and September 2020 was conducted at 30 mW with five accumulations of 30 s integration time and using the 1800 grooves/mm grating to achieve maximum spectral resolution ( $0.54\text{ cm}^{-1}$ ). To improve the quality of the lower density data ( $0\text{--}0.1\text{ g/mL}$ ), analyses were conducted in November 2020 at 60 mW and integration times up to 90–100 s and up to five accumulations. Pressure was sampled every second by the transducer probe's software with precise time stamps that were associated with each analysis. Temperature was recorded manually every 20–30 s during each analysis.

All collections were done in a single spectral window ( $1057\text{--}1608\text{ cm}^{-1}$ ) and Neon (Ne) spectra were collected immediately before and after each analysis using 45 s integration time and three accumulations to correct for non-linearity of the Raman shift axis (details in Section

5.1). We do not collect simultaneous Ne emission lines as they can result in interference between Raman bands and an overall reduction of Fermi diad peak intensities, harming the fitting procedures.

The  $\text{CO}_2$  analyses were conducted at two separate temperatures: “room temperature” of  $24.77\text{ }^{\circ}\text{C}$ , and  $37\text{ }^{\circ}\text{C}$  to homogenize coexisting liquid and vapor  $\text{CO}_2$  into a single supercritical phase ( $31.1\text{ }^{\circ}\text{C}$  is the critical temperature of pure  $\text{CO}_2$ ). In both cases, temperature was held constant using the Peltier thermoelectric stage under the  $\text{CO}_2$  chamber. The  $37\text{ }^{\circ}\text{C}$  analyses were conducted in 0.01 MPa increments from 0.035 to 0.1 MPa, 0.5 MPa increments from 0.1 to 7 MPa, 0.1 MPa increments from 7 to 11 MPa (with a few additional data points between 8 and 9 MPa), and 1 MPa increments from 11 to 34 MPa. Special care was taken to ensure adequate data coverage and high accuracy and precision was obtained for mid-densities in the critical region ( $\sim 6.5\text{--}10.5$  MPa or  $0.2\text{--}0.7\text{ g/mL}$ ). For  $24.77\text{ }^{\circ}\text{C}$ , increments of 0.01 MPa were used from 0.035 to 0.1 MPa, 0.25 MPa increments from 0.1 to 6.25 MPa, 0.5 MPa increments from 7 to 11 MPa, and 1 MPa increments from 11 to 34 MPa.

Previous densimeters (Fall et al., 2011; Kawakami et al., 2003; Rosso and Bodnar, 1995; Song et al., 2009; Wang et al., 2011; Yamamoto and Kagi, 2006) had rather sparse sampling in the critical region with large uncertainties. For example, Kawakami et al. (2003) measured only seven points in the critical region at temperatures between 58 and  $60\text{ }^{\circ}\text{C}$  while Wang et al. (2011) measured 32 points in the critical region at  $40\text{ }^{\circ}\text{C}$ . Song et al. (2009) generated their  $\text{CO}_2$  data from synthetic inclusions in fused silica capillaries, which included just four points in the critical region. Fall et al. (2011) had a large dataset in the critical region (18 points between  $0.22$  and  $0.7\text{ g/mL}$ ); however, their FDCA design resulted in potentially large uncertainties in the temperature of the  $\text{CO}_2$  fluid as the temperature was measured outside of the  $\text{CO}_2$  chamber. Additionally, the Fall et al. (2011) densimeter conducted measurements at a variety of temperatures from  $35$  to  $-10\text{ }^{\circ}\text{C}$ , and all of this data was included in the calibration and regression. This may have imbalanced the regression towards the liquid and vapor regions, and also disregarded any potential effect of the temperature on the separation of the Fermi diad.

To improve on these previous densimeters, we paid special attention and care to the critical region, increasing the sampling rate (48 points between  $0.22$  and  $0.7\text{ g/mL}$ ) as well as precision and accuracy of measurements ensuring that temperature varied by no more than  $\pm 0.02\text{ }^{\circ}\text{C}$ . We also varied the sampling frequency by pressure range to ensure an approximately equal number of data points in each sub-region (low, mid, and high-density) so as to not skew the calibration. As will be discussed later, we also separated the densimeter into three regions corresponding to the low-density (vapor), mid-density, and high-density regions to provide a better overall fit to the data. Additionally, to account for slight differences in the Fermi diad split due to temperature, we separated the regressions for room temperature ( $24.77\text{ }^{\circ}\text{C}$ ) and supercritical temperature ( $37\text{ }^{\circ}\text{C}$ ).

#### 3.2. Raman data post-processing

To correlate  $\text{CO}_2$  density with the Fermi diad separation in the Raman spectrum, we first determined the densities of each analysis. Pressure was sampled every second by the transducer probe's software with precise time stamps, and we used the median value of pressure over the time interval for each analysis. Temperature was also taken as the median of 20 s sampling frequency for each analysis. Peak positions were found using a Lorentzian-Gaussian least-squares minimizing peak fitting procedure in MATLAB and the data was not smoothed prior to fitting. This peak fitting program assumes a horizontal line for the baseline and uses the first point in the fitting window for this baseline subtraction. We selected the fitting window carefully to include both the Fermi diad and surrounding flat spectral region. For comparison, we also processed a few of these spectra using Voigt functions in the open source software Fityk (Wojdyr, 2010; <http://fityk.nieto.pl/>) and found similar results to our MATLAB peak fits.

It had been suggested in previous studies that the absolute value of the peak splitting of the Fermi diad is sufficiently small to not be affected by any non-linearity of the instrument's monochromator (Lamadrid et al., 2017; McCreery, 2005). However, it is apparent that variations in the Fermi diad separation ( $\Delta\text{CO}_2\text{uncorrected}$ ) exist for data collected on different days but at the same P-T conditions (Fig. 4a and c). On the WITec Alpha 300R, linearity is defined using the laser line (i.e.,  $0\text{ cm}^{-1}$ ) and a silicon peak ( $\sim 520\text{ cm}^{-1}$ ). However, the linearity is then only valid between those specific lines. Lin et al. (2007) suggested that non-linearity of the Raman shift axis may be compensated for by selecting a Raman band close to the spectral region of interest. Therefore, to compensate for the non-linearity of our instrument we calibrated our data using two known Ne emission lines ( $1122.7763$  and  $1453.2539\text{ cm}^{-1}$ ) that bracket the Fermi diad with sufficient intensity following the method described in Lamadrid et al. (2017). These emission lines are specific to our laser excitation wavelength of  $531.885\text{ nm}$  and should be recalculated if a different source is to be used. We should also note that the lower Ne emission line ( $\sim 1122\text{ cm}^{-1}$ ) appears as a double-peak on the Raman spectrum because there is an additional, weaker Ne line at  $\sim 1120\text{ cm}^{-1}$ . However, at the  $1800\text{ grooves/mm}$  grating, the resolution is high enough that both peaks can be fit and resolved. The corrected

Fermi diad separation ( $\Delta\text{CO}_2\text{corrected}$ ) can then be calculated using the observed and real separation of the Ne emission lines through the following equation (Lamadrid et al., 2017):

$$\Delta\text{CO}_2\text{corrected} = \left( \frac{\Delta\text{Ne}_{\text{real}}}{\Delta\text{Ne}_{\text{observed}}} \right) * \Delta\text{CO}_2\text{uncorrected} \quad (1)$$

where  $\Delta\text{CO}_2\text{corrected}$  is the corrected separation of the Fermi diad,  $\Delta\text{Ne}_{\text{real}}$  is the known separation of the selected Ne emission lines,  $\Delta\text{Ne}_{\text{observed}}$  is the separation of the same Ne emission lines measured from each Raman spectrum and  $\Delta\text{CO}_2\text{uncorrected}$  is the measured separation of the Fermi diad.

The result of the correction (Fig. 4b and d) suggests that the observed difference in Fermi diad separation for a single density measured on different days (Fig. 4a and c) is indeed the result of non-linearity and any densimeter should be corrected using a similar technique. The Lamadrid et al. (2017) densimeter accounts for non-linearity but is only valid for  $\text{CO}_2$  vapor densities ( $<0.2\text{ g/mL}$ ). Ours is the first  $\text{CO}_2$  densimeter spanning the entire range of  $\text{CO}_2$  densities that includes a correction for non-linearity using Ne emission lines. The Wang et al. (2011) densimeter also corrected for non-linearity but did so using two bracketing benzonitrile bands.

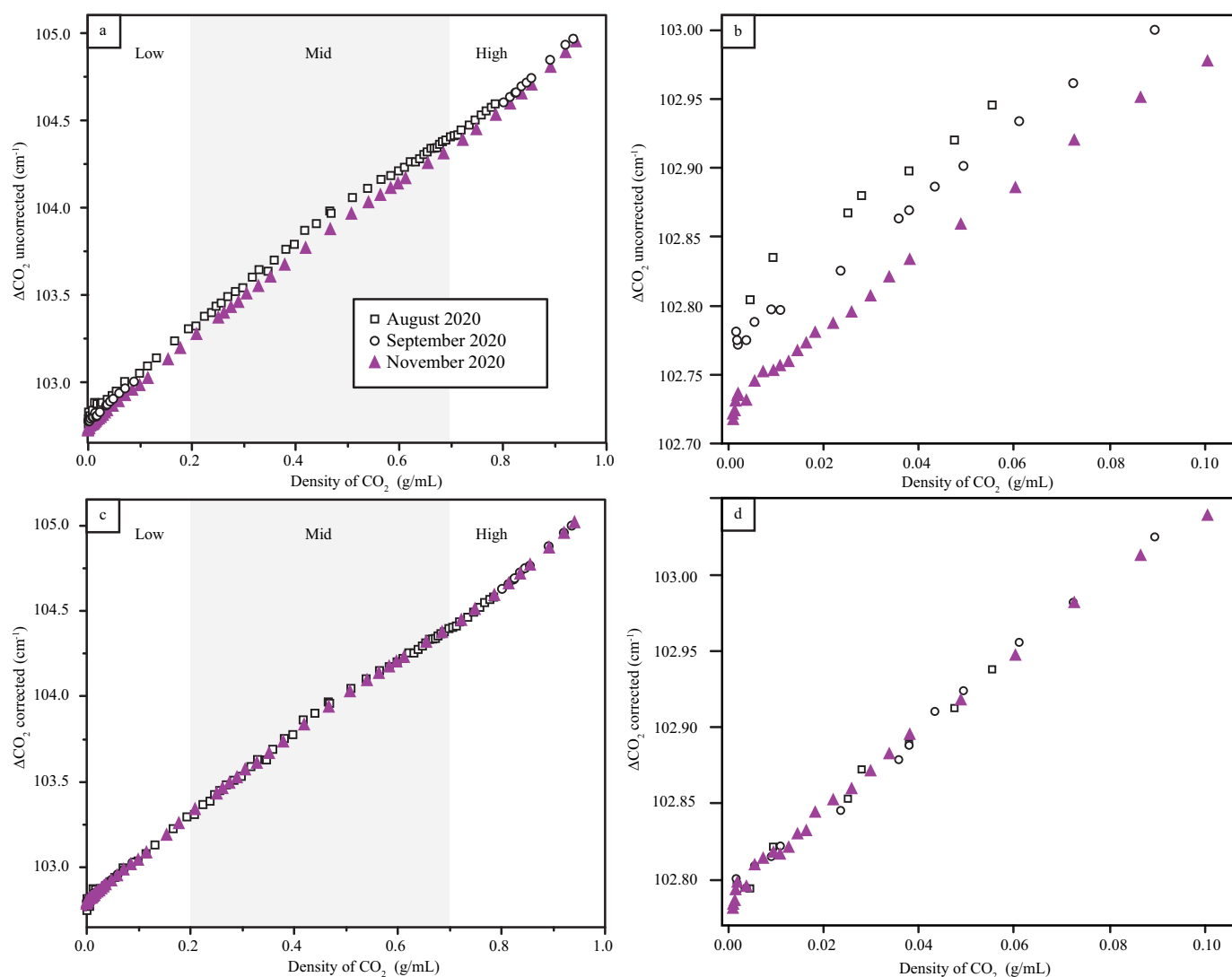


**Fig. 4.** Comparison between uncorrected data for Fermi diad separation (a, b) and data corrected for non-linearity of the Raman shift axis using Ne emission lines (c, d). Panels a and c show the full range of the calibration and panels b and d are zoomed in on the ultra-low-density vapor region (0.001–0.1 g/mL). Shaded regions show mid-densities which require homogenization into a supercritical phase to be measured - otherwise two phases with two separate densities (Liquid and Vapor) are present. Regions are labeled low-density (Low), mid-density (Mid) and high-density (High).



## 4. Results

A total of 229 data points were obtained, 96 for 24.77 °C (standard deviation of 0.015 °C) and 133 for 37 °C (standard deviation of 0.03 °C) during multiple sessions. During a preliminary set of experiments, we conducted room temperature measurements for high and low densities with no Peltier plate. We observed that the measured temperature throughout the experiment varied by up to 2 °C potentially resulting in up to 0.02 g/mL uncertainty at high densities (0.75–1 g/mL; Fig. 3a–b). We found that this potential error was easily reduced by using the thermoelectric Peltier plate to maintain a constant temperature of ~24 °C. For this reason, we used the Peltier stage to maintain temperature stability both at room temperature (24.77 °C) and 37 °C.

Spectra were also collected for capillary tubes of densities between 0.009 and 0.09 g/mL as internal standards at both 24 °C and 37 °C. These were used to test the sensitivity of the peak positions to laser power and integration time and ensure that we collected the best possible spectra for the low-density region (Fig. 5). Note that the box plots of August and September data show much larger spread in the Fermi diad separation in the ultra-low-density region (0.001–0.1 g/mL) than those of November because we doubled the laser power and increased collection times for the November session. Capillary densities plotted on Fig. 5 are calculated from the mass of CO<sub>2</sub> loaded into the capillary tubes and have not been corrected based on our new calibration.

All CO<sub>2</sub> data were corrected for non-linearity using Eq. 1. The measured distance between the two Ne lines (1122.7763 and 1453.2539 cm<sup>-1</sup>) used for our calibrations span a range of  $\pm 0.015$  cm<sup>-1</sup>, with a standard deviation of 0.008 cm<sup>-1</sup>. The full dataset for this calibration can be found in supplementary material and is plotted in Fig. 4a–b.

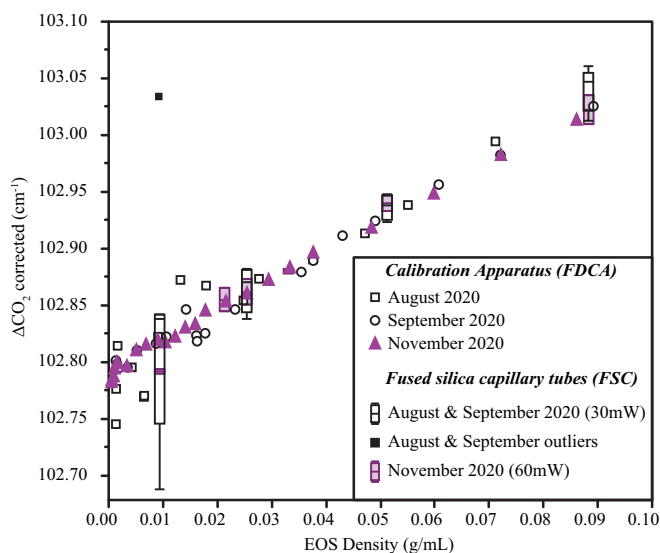


**Fig. 5.** Corrected Fermi diad separation plotted against the calculated densities based on experimental P-T data. November 2020 data was acquired with revisited instrumental parameters to optimize the signal for very low densities (laser power was doubled and collection times significantly increased compared to August and September data). Fused silica capillaries collected during the same sessions are plotted as box plots. Outlier box plots were calculated using SAS® JMP software and indicate the median, interquartile range (InR), whiskers (1st quartile-1.5\*InR or 3rd quartile +1.5\*InR) and outliers (further than whiskers). Note that the spread in the data for ultra-low densities is significantly reduced in the November data. Capillary densities are based on mass of CO<sub>2</sub> loaded into the tubes and have not been corrected to our calibration here.

### 4.1. Uncertainty analysis

The density for each P-T analysis was calculated using the NIST online calculator (<http://webbook.nist.gov/chemistry/fluid/>) based on the Span and Wagner (1996) EOS for CO<sub>2</sub>. We can use the EOS to understand expected uncertainty distributions, how they may manifest in our data (Fig. 6a) and how they further translate to potential estimations of the CO<sub>2</sub> contents of melt inclusions (Fig. 6b). These calculations were done for 37 °C to model the conditions in our experiments and include mid-densities. However, the distribution of potential error in the high-density and low-density vapor region is the same regardless of temperature. An error of  $\pm 0.05$  g/mL (which can also be caused by about  $\pm 0.3$  °C error in temperature measurements for the critical region) translates to different potential error at different densities (Fig. 6a). Such an error in the density would represent no more than 11% total potential error at high densities (i.e., 0.9 g/mL), which may be acceptable. However, the same relative error would represent 100% total potential error at low density such as 0.1 g/mL and 22% in the mid-density region. Additionally, this could result in hundreds to thousands of ppm uncertainty in CO<sub>2</sub> contents for melt inclusions depending on the % volume occupied by the bubble (Fig. 6b), yielding significant errors in determinations of saturation pressure. We further estimated the error distributions for uncertainties of  $\pm 0.01$  g/mL and  $\pm 0.001$  g/mL and compared these distributions to the compounded uncertainties in our data due to both pressure and temperature (Fig. 6a). Our data shows no more than 5% density uncertainty in the worst case in the critical region, which is the most sensitive to uncertainty, and this would correspond to a total error of at most 350 ppm in the CO<sub>2</sub> content of the bubble for densities of 0.4–0.5 g/mL and a 5% volume fraction bubble (Fig. 6b).

Additionally, we estimated the effect of uncertainty in pressure and temperature measurements on density at specific P-T conditions of our experiments along with the uncertainty in the Fermi diad separation as a result of repeated analyses (black bars on Fig. 7). Uncertainty in pressure is shown in Fig. 7e–f). Note that the compounded uncertainty on the density of our samples is smaller than the symbols except in the critical region (Fig. 7d) but never exceeds a total uncertainty of 0.017 g/mL. To estimate the uncertainty in the Fermi diad split position of our samples, we took the mean value of repeated sets of measurements (corrected for non-linearity by Ne) and present the range of error for these mean values as the minimum and maximum values from these repeated analyses (plotted as black bars in Fig. 7a–d). Except for extremely low densities (Fig. 7c) which show variations of up to  $\pm 0.045$  cm<sup>-1</sup> and mid-densities (Fig. 7d) with maximum variation of  $\pm 0.015$  cm<sup>-1</sup>, all other variations in Fermi diad separation are smaller than the symbols and smaller than  $\pm 0.005$  cm<sup>-1</sup>.

### 4.2. Construction of the new densimeter equations

Before constructing a new CO<sub>2</sub> densimeter with our new highly precise data, we first consider the effect of temperature on the results (Fig. 8a). At lower densities (vapor region; Fig. 8c–d), temperature has a relatively small effect on the separation of the Fermi diad. At these vapor densities, the data from both temperatures show good agreement up to ~0.1 g/mL (Fig. 8d), which corresponds to a pressure of about 3 MPa (Fig. 8c). However, at higher densities (i.e., CO<sub>2</sub> liquid), the effect is much more pronounced. This is because the isochores for CO<sub>2</sub> liquid have much steeper slopes (Fig. 1c; Diamond, 2003; Fall et al., 2011; Hollister, 1981) than those in the vapor region, so a small change in temperature has a larger effect on density at higher densities. Previous studies have largely dismissed this small, albeit existent, effect on the lower density region (Fig. 8d). However, because of this effect, we chose to separate the data into two separate sets of equations, one for data at a sub-critical temperature of 24.77 °C and another set for data collected at 37 °C (above critical temperature).

Furthermore, we split the data into three different density regions (Fig. 8b) corresponding approximately to CO<sub>2</sub> vapor (0–6.25 MPa or ~

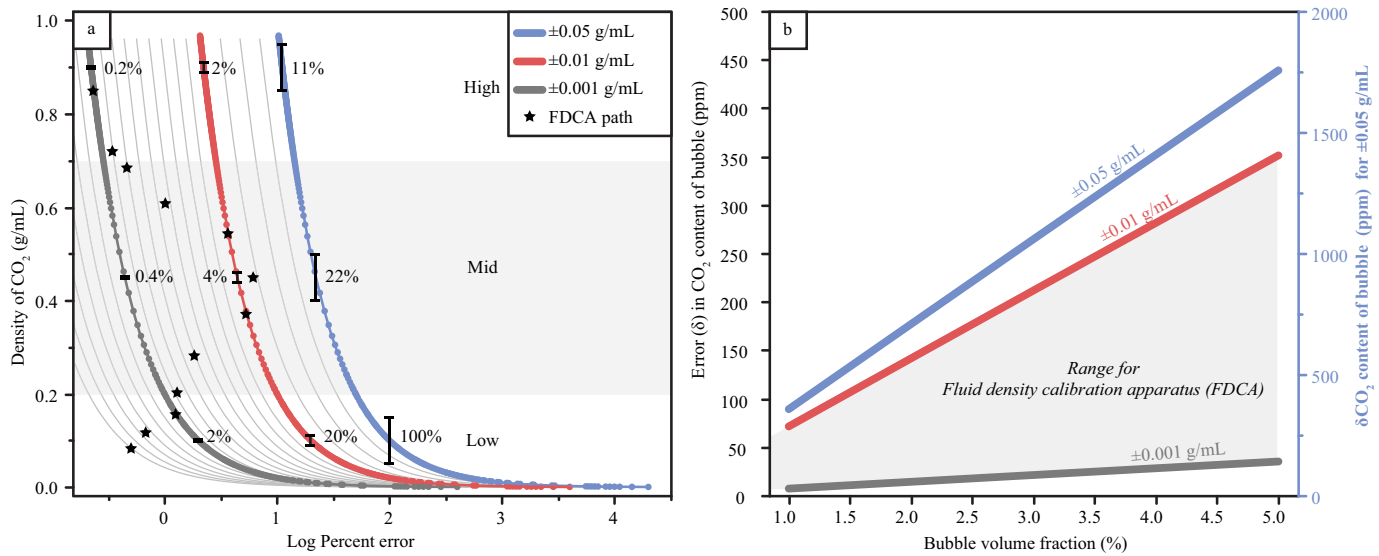


**Fig. 6.** Assessment of uncertainties for a given error in density. a) Relative % error in density at different CO<sub>2</sub> densities for different absolute uncertainties in the density. Note that the approximate error path of our samples (using empirically propagated P-T uncertainty on the density through the EOS) is plotted as black stars. In the worst-case scenario, error in our samples does not exceed 5% in the critical region and is much less in the high- and low-density regions. b) Error in CO<sub>2</sub> content of melt inclusion bubbles calculated for different uncertainties in density and as a function of the volume% occupied by the bubble.

0–0.17 g/mL), liquid CO<sub>2</sub> (9.5–35 MPa or ~0.65–1.0 g/mL) and densities that can only be measured as supercritical CO<sub>2</sub> fluid at the two temperatures considered here (5–11 MPa or ~0.12–0.72 g/mL). The regions covered by the equations are purposefully overlapped so that in the future the mid-density and high-density equations can be corrected using the same standards as for the lower density equation and avoid the need to run the calibration for every analytical session. We note that the equations proposed should only be used specifically for the aforementioned conditions (i.e., Eqs. 2, 3 and 4 should only be used for neon-corrected data acquired at 37 °C and shifted using CO<sub>2</sub> standards also acquired at 37 °C). Additionally, due to the impossibility of overlap for the room temperature equations, the room temperature high-density equation proposed in this study should only be used when appropriate high density CO<sub>2</sub> standards are available to correct it for individual analytical sessions.

CO<sub>2</sub> density was fit as function of the corrected separation of the Fermi diad ( $\Delta\text{CO}_2\text{corrected}$ ) for three different regions at 37 °C (Fig. 9a–c) and two regions for 24.77 °C (Fig. 9d–e) using statistical software package JMP from SAS. For all regions, linear regressions as well as 2nd and 3rd degree centered fits (predictors are rescaled by subtracting the mean) were performed, and the residuals as well as the significance of the fit parameters as expressed by their *p*-values were compared.

For the high-density region at both 37 °C and 24.77 °C (Fig. 9a and d) the linear regressions displayed residuals with non-random parabolic distributions, indicating that a higher order polynomial would be more suited to the data. A 2nd degree polynomial was found to be a best fit for this region for both cases while the 3rd order parameter of the 3rd degree polynomial was found to be statistically non-significant (*p*-value > 0.05).

For the mid-density region of the 37 °C dataset (Fig. 9b), 3rd order polynomial was found to be the best fit. For this region, both the linear fit and 2nd degree polynomial showed non-random residual distributions, while all parameters were statistically significant for the 3rd order polynomial.

Finally, the low-density vapor regions for both 37 °C and 24.77 °C were best represented by linear regressions (Fig. 9c and e). Residuals plots were randomly distributed, and higher order polynomial parameters were found to be statistically non-significant (S3-supplementary materials).

The equations are as follows:

1) For the 37 °C dataset

a. High-density region (Fig. 9a; ~0.65–1.0 g/mL)

$$\rho_{\text{CO}_2} = -43.62113 + 0.4246088\Delta\text{CO}_2\text{corrected} - 0.1527029(\Delta\text{CO}_2\text{corrected} - 104.58)^2 \quad (2)$$

$$R^2 = 0.998968; \text{RMSE} = 0.002862; \text{p-value} < 0.0001$$

b. Mid-density/critical region (Fig. 9b; ~0.12–0.72 g/mL)

$$\rho_{\text{CO}_2} = -46.17504 + 0.448773\Delta\text{CO}_2\text{corrected} + 0.0773642(\Delta\text{CO}_2\text{corrected} - 103.848)^2 + 0.0343283(\Delta\text{CO}_2\text{corrected} - 103.848)^3 \quad (3)$$

$$R^2 = 0.999682; \text{RMSE} = 0.00358; \text{p-value} < 0.0001$$

c. Low-density region (Fig. 9c; ~0–0.17 g/mL)

$$\rho_{\text{CO}_2} = -40.22688 + 0.3913402\Delta\text{CO}_2\text{corrected} \quad (4)$$

$$R^2 = 0.998041; \text{RMSE} = 0.002245; \text{p-value} < 0.0001$$

2) For the 24.77 °C dataset

a. High-density region (Fig. 9d; ~0.7–1.0 g/mL)

$$\rho_{\text{CO}_2} = -40.08933 + 0.3907468\Delta\text{CO}_2\text{corrected} - 0.1655607(\Delta\text{CO}_2\text{corrected} - 104.776)^2 \quad (5)$$

$$R^2 = 0.999558; \text{RMSE} = 0.001557; \text{p-value} < 0.0001$$

b. Low-density region (Fig. 9e; ~0–0.22 g/mL)

$$\rho_{\text{CO}_2} = -38.26455 + 0.3722442\Delta\text{CO}_2\text{corrected} \quad (6)$$

$$R^2 = 0.997364; \text{RMSE} = 0.002887; \text{p-value} < 0.0001$$

All data associated with this calibration is included in the supplementary materials as an Excel table. Note that these equations should only be used on unknown data within the calibrated parameters and for data acquired with the same experimental and instrumental configurations. If another instrument is used, an FDCA of the same design should ideally be built for that instrument or at least the unknown sample data

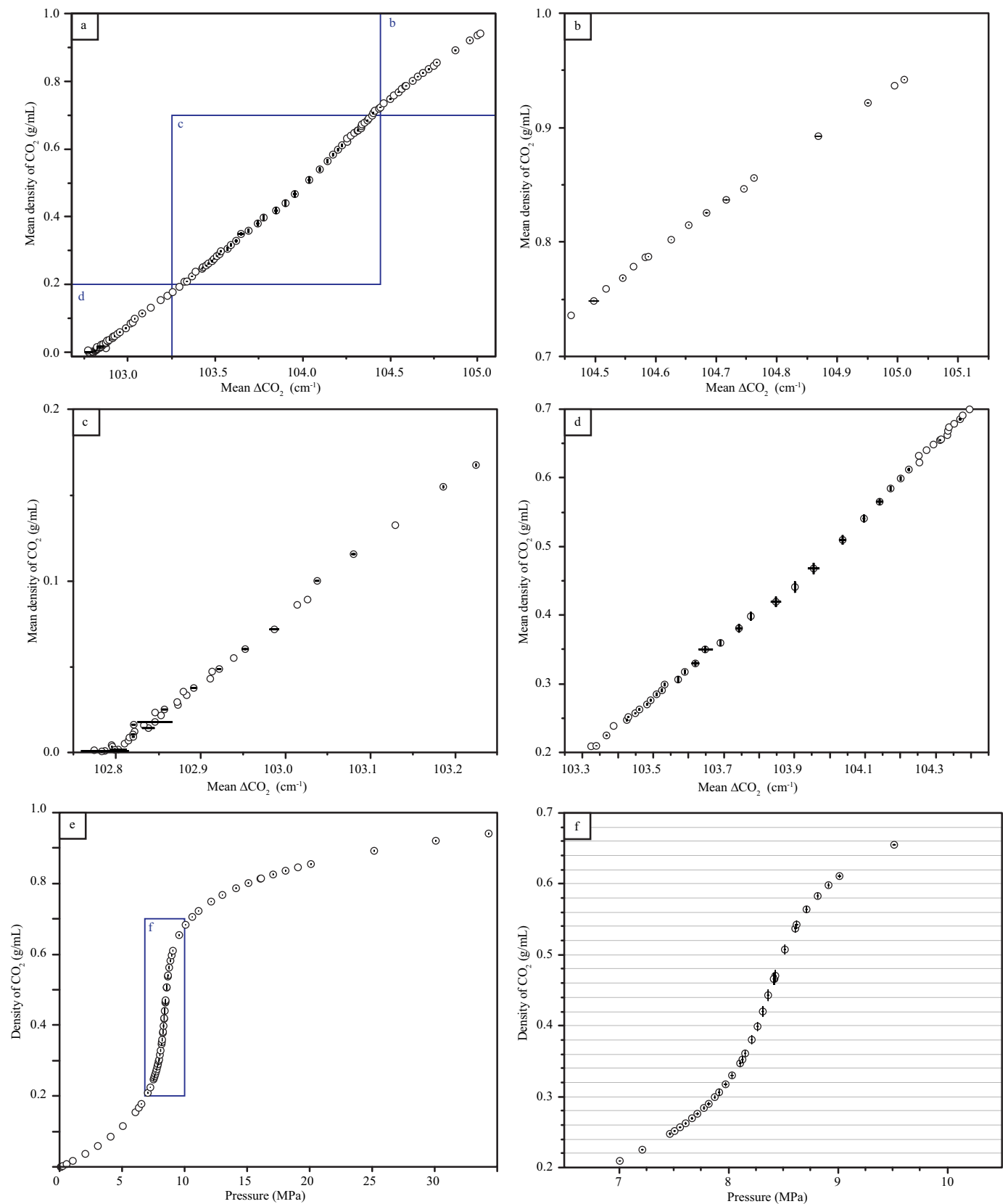


**Fig. 7.** Empirically propagated P-T uncertainty on the density and uncertainties in Fermi diad separation for means of repeated measurements. Data points shown are averaged density and averaged  $\Delta\text{CO}_2$  from different runs of the FDCA calibration, when available. The uncertainty on the density was not calculated for every single data point but instead for a range of relevant values, and we assume that points without uncertainties have uncertainties bracketed by the nearest values. Note that except in the mid-density region and extremely low-density region, uncertainties are smaller than the symbols. Panels b, c, and d are zoomed in plots for the high-density, mid-density and low-density regions, respectively. Errors in the pressure are shown in panels e and f.

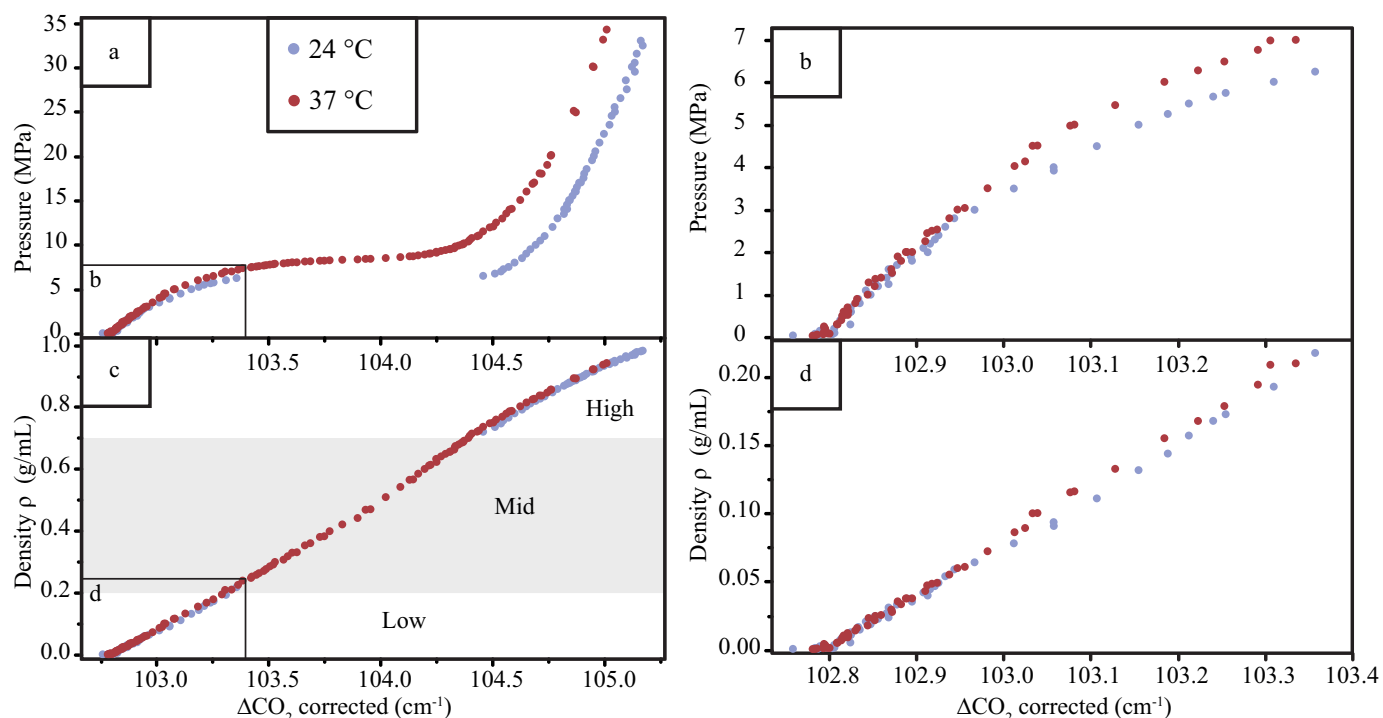


**Fig. 8.** Variations in Fermi diad separation due to changes in the temperature of the calibration as functions of pressure and density of CO<sub>2</sub>. Panels a and c show the full range of the calibrations at 24.77 °C and 37 °C. The effect is more important at higher densities but appears in the lower density data at >0.1 g/mL (b and d).

should be corrected for non-linearity of the Raman shift axis and then shifted using known density standards such as fused silica capillaries prior to calculating densities (see method in Allison et al., 2021). As Lamadrid et al. (2017) and others have shown, large errors of more than 0.1 g/mL can occur as a result of using a densimeter not calibrated for a specific instrument, laser wavelength and/or gratings (see Fig. 7 in Lamadrid et al., 2017).

## 5. Discussion

### 5.1. Comparison with previous densimeters

One of the major strengths of our modified FDCA and resulting dataset is excellent temperature accuracy, yielding very well constrained EOS-calculated densities. As a result of this low error on the EOS-calculated density of each measurement combined with separate equations for different density ranges, our densimeters and calibration dataset agree very closely with one another (Fig. 10). The maximum difference in densimeter-calculated and EOS-calculated densities is 0.011 g/mL for this study at 37 °C. For previously published densimeters, differences between the EOS-calculated and densimeter-predicted densities are much larger (Fig. 10). For example, the differences are roughly 0.04 g/mL for Kawakami et al. (2003) and Wang et al. (2011), with one outlier at 0.07 g/mL in the Kawakami et al. (2003) dataset. These differences tend to be largest in the mid-density region, which perhaps suggests that some of these differences might be explained by temperature uncertainties (which have been significantly reduced in this study).

In Fig. 11a we show the results of calculating the density of the 37 °C calibration dataset from our study using previously published densimeters. However, we note that each of the previously published non-linear densimeters were calibrated from a mixed-temperature dataset; i.e., measurements at temperatures  $\geq 35$  °C for densities  $\sim 0.2$  to 0.7 g/mL but typically at room temperature for all other densities (temperatures from previous studies discussed in Section 3.1). As shown in Fig. 8, at isochoric conditions, increasing temperature causes the Fermi diad

separation to become smaller, which would impact the calibration of a densimeter. To examine how temperature might impact these comparisons, we also include a 3rd order polynomial mixed-temperature densimeter calibrated from our data in Fig. 11a. This mixed-temperature densimeter was calibrated using 24 °C data at densities <0.22 g/mL and >0.7 g/mL and 37 °C data in the mid-density region.

Overall, Fig. 11a shows that these other densimeters predict a wide range of densities for each of our data points. Large differences are expected, because these other densimeters were not specifically calibrated for the instrument and analytical settings we used to collect this data. However, this calculation shows interesting trends predicted by the previously published densimeters that warrant further discussion. In particular, most of the other densimeters, including the mixed-temperature equation we calibrated for comparison only, tend to show larger differences from the EOS-calculated density in the mid-density region.

For better comparison of these differences, in Fig. 11b we shift each of the densimeters by a 3-point linear regression using calibration points from the 37 °C dataset at 0.0473, 0.155 and 0.837 g/mL (cyan stars). This shift is a simple correction to account for the offsets observed between densimeters (e.g., Lamadrid et al., 2017) that result from differences between instruments and analytical settings. These shifted density differences show a clear discrepancy between densimeters in the mid-density region. Fig. 11b illustrates that only some of the differences might be explained by calibration from a mixed-temperature dataset, as the mixed-temperature equation we calibrated from our data only shows  $\sim 0.02$  g/mL difference from the EOS-calculated densities for the 37 °C dataset.

Because all of the previously published non-linear densimeters were calibrated from mixed-temperature data, we also compare densimeter-predicted and EOS-calculated density for a mixed-temperature dataset from our study (Fig. 11c). This is the dataset we used to calibrate a mixed-temperature densimeter for Fig. 11a-b and includes 24 °C data at densities <0.22 g/mL and >0.7 g/mL and 37 °C data in the mid-density region. For easier comparison between results from different densimeters, we again shift these results using a 3-point (cyan stars) linear



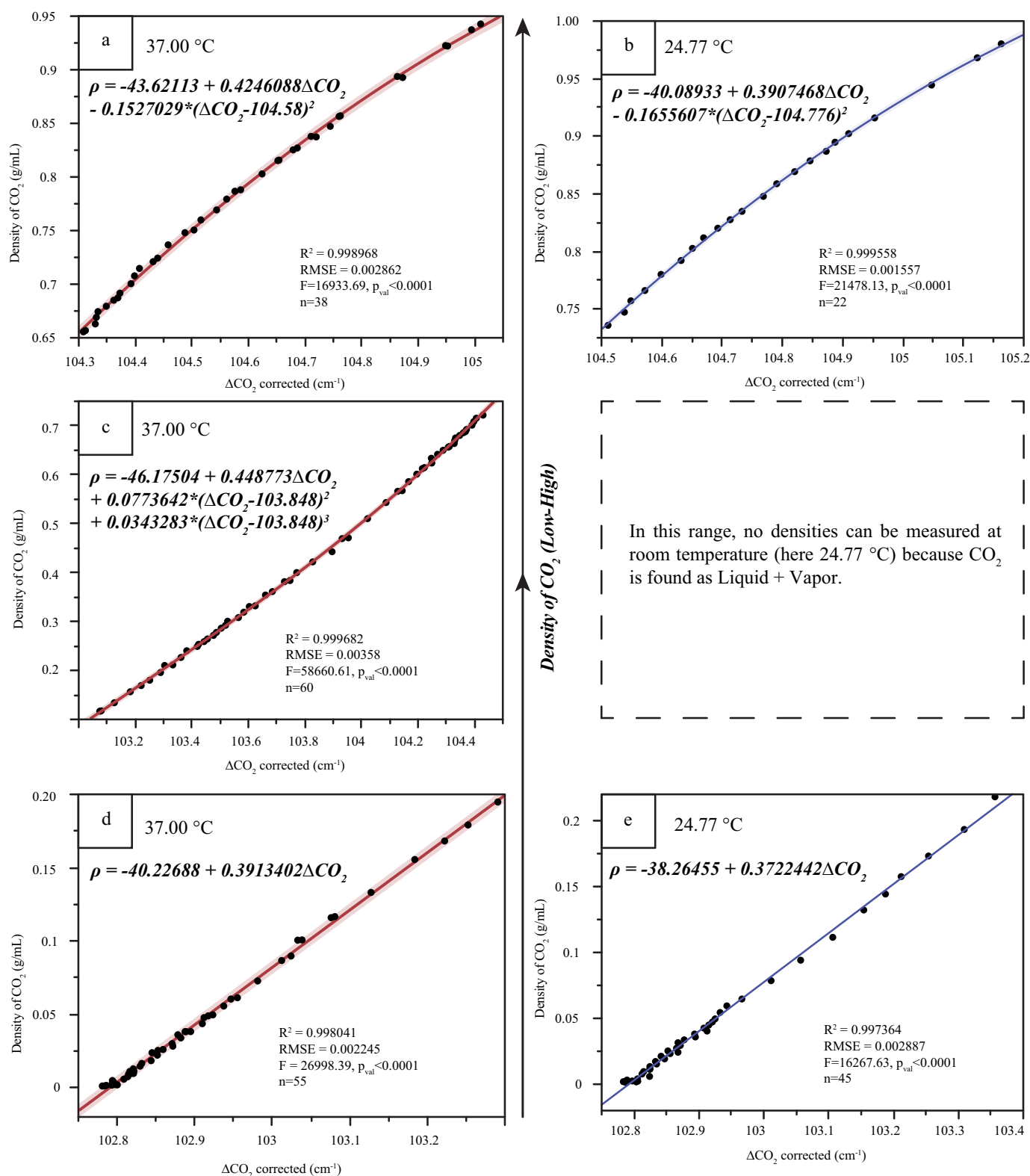


**Fig. 9.** Regression parameters and new densimeter equations. a, c, d) Equations for the densimeter at 37 °C from high to low densities. b, e) Equations for the densimeter at 24.77 °C from high to low densities.

regression in Fig. 11d. The same overall trends are observed in Fig. 11b and Fig. 11d, with large differences in the mid-density region, although the maximum differences predicted by each densimeter are all ~0.01 g/mL lower in Fig. 11d compared to Fig. 11b.

We note that the magnitude of these density differences might

change slightly as a result of how the offsets between densimeter are corrected; i.e., what densities are used to shift each densimeter. In Fig. 11e, the difference results from Fig. 11c (mixed-temperature data) are shifted using only low density datapoints at 0.009, 0.111, and 0.193 g/mL. This results in excellent agreement between densimeters at low

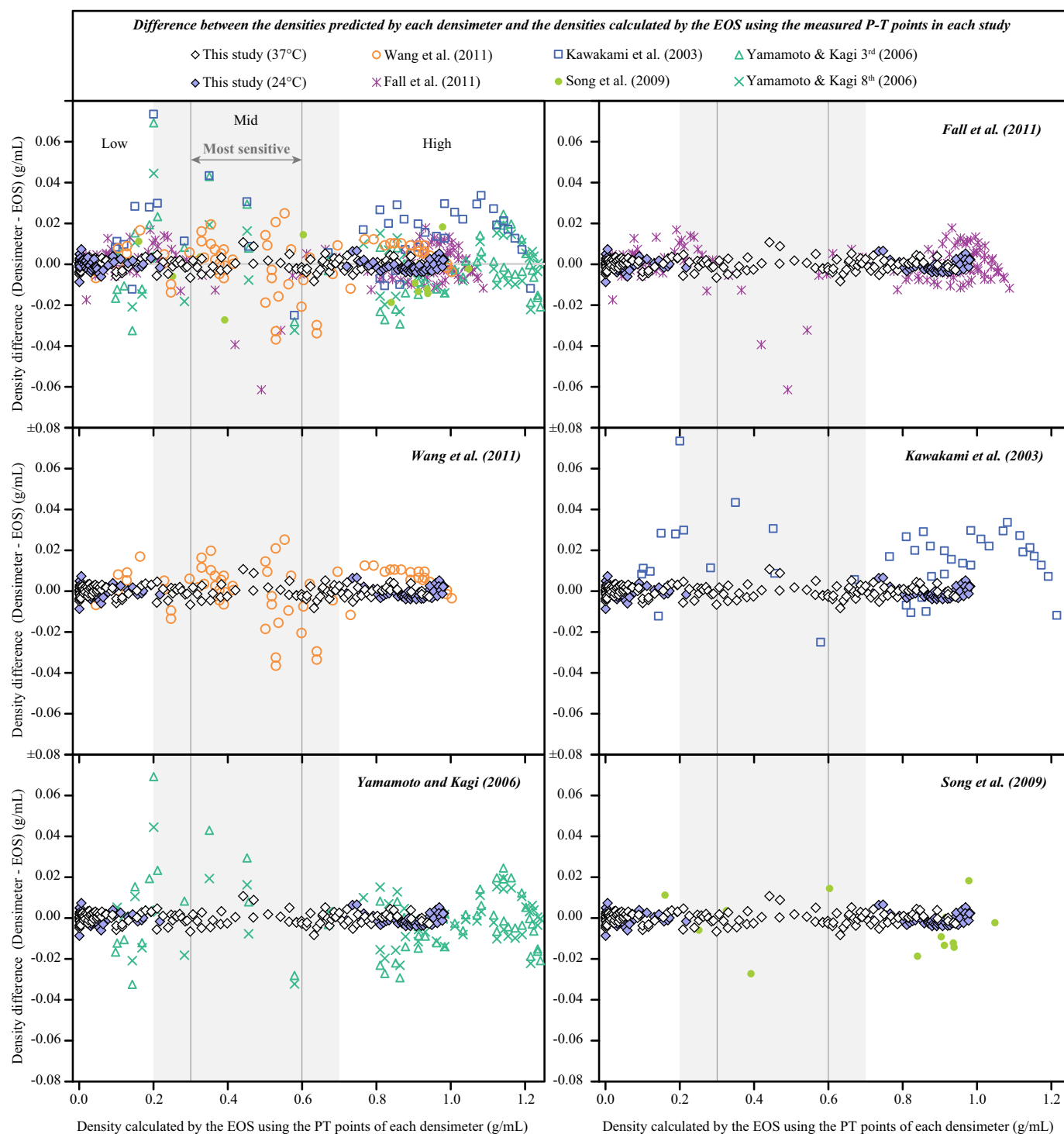


**Fig. 10.** Comparison of how well different densimeters agree with their calibration datasets. Values of Fermi diad separation and EOS-calculated density for the other studies come from the compilation included in Lamadrid et al. (2017). Note that EOS-calculated values for the Fall et al. (2011) dataset were not provided in the original study (EOS-calculated density was only shown in their Fig. 4b) or the compilation from Lamadrid et al. (2017). For this study, we calculated densities for the Fall et al. (2011) dataset using the EOS used in that study (Span and Wagner, 1996) from the pressures and temperature values reported in their supplementary material, which were primarily reported as integer values. Regions are labeled low-density (Low), mid-density (Mid) and high-density (High).

densities, but much larger differences at mid- and high-densities ( $>0.1$  g/mL at high densities). Another example is shown in Fig. 11f, where the difference results from Fig. 11c (mixed-temperature data) are shifted using data at the upper and lower ends of our dataset. The maximum differences observed in Fig. 11d and f are quite similar, though the results are not identical. Overall, this exercise suggests that corrections for offsets between densimeters require CO<sub>2</sub> standards across the entire

range of the densities of interest.

Previous studies have acknowledged the differences in published densimeters and proposed many explanations for the discrepancies. One of the reasons invoked is differences in the EOS used to calculate the densities from P-T data; for example, Rosso and Bodnar (1995), Yamamoto and Kagi (2006), and Kawakami et al. (2003) did not use the Span and Wagner (1996) EOS. However, Lamadrid et al. (2017) demonstrated

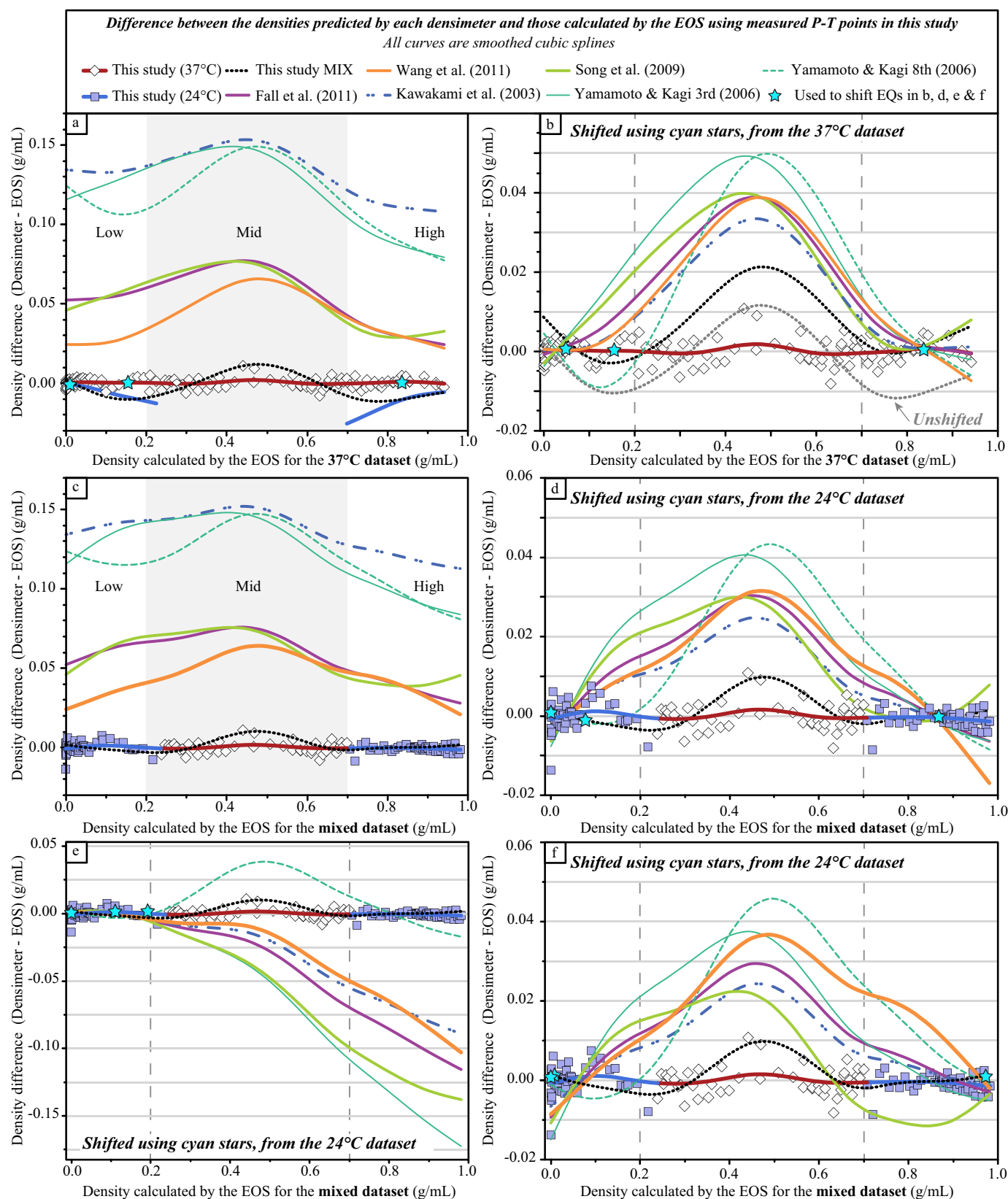


**Fig. 11.** Comparison of results from densimeters. a) Differences in the density predicted by densimeters for the 37 °C data in our study compared to values calculated using the EOS from [Span and Wagner \(1996\)](#). b) Difference data from panel a shifted using 3-point (cyan stars) linear regressions of 37 °C data. c) Differences in the density predicted by densimeters for a mixed-temperature dataset from our study compared to values calculated using the EOS from [Span and Wagner \(1996\)](#). The mixed-temperature dataset includes 24 °C data at densities <0.22 g/mL and > 0.7 g/mL and 37 °C data in the mid-density region. d-f) Difference data from panel c shifted using three different 3-point (cyan stars) linear regressions of points from the mixed dataset. Note that the “hat”-shaped trends in panels b, d, and f suggest that previously published densimeters would predict much higher densities than the EOS for the mid-density data we measured even after shifting. (For interpretation of the references to colour in this figure legend, the reader is referred to the web version of this article.)

that the differences in density calculated at the same temperature from 0.1 to 200 MPa using the [Stern and Pitzer \(1994\)](#) and [Span and Wagner \(1996\)](#) EOS are about 1%, with a standard deviation of 0.43% and therefore unable to explain the large discrepancies in density produced by the equations ([Fig. 11a-b](#)).

Other reasons for differences between densimeters include hardware construction differences (which would explain the large discrepancies between instruments observed by [Lamadrid et al., 2017](#)), or room temperature fluctuations that can cause thermal contraction and expansion of the spectrometers ([Fukura et al., 2006](#); [Gaufrès et al., 1995](#); [Mestari et al., 1997](#)). However, overall, the equations from previous publications largely agree in trends but are offset by significant margins. This resembles the discrepancies observed by [Lamadrid et al. \(2017\)](#) when using different laser excitation wavelengths, gratings and instruments, hence is a likely explanation for the offset between the trends ([Fig. 11a and c](#)). Still, this explanation fails to account for the large increased differences between densimeters in the critical region compared with the low and high-density regions ([Fig. 11b and d](#)).

As mentioned previously in [Section 2.2](#), temperature uncertainties can have significant impact on the quality of the data in the critical region ([Fig. 3c](#)). It is perhaps unsurprising that the general trend of the error in CO<sub>2</sub> density resulting from uncertainty in the temperature is similar to that of the uncertainty produced by calculating densities using previously published densimeters and normalizing the error to the EOS ([Fig. 11](#)). Pressure can also have the same effect; however, pressure is typically well-constrained during FDCA experiments and is easily measured with high precision and accuracy. For this reason, it is likely that the uncertainty in the mid-densities of previously published densimeters results from the large uncertainty in the temperature measurements. This highlights the importance of measuring the temperature of the fluid inside the CO<sub>2</sub> chamber instead of the surrounding enclosure. It also suggests that temperature should be measured using a high accuracy thermometer calibrated for the analysis temperatures rather than lower accuracy thermocouples.

## 5.2. New densimeter test on unknown samples: case study of Pico do Fogo volcano, Cabo Verde Archipelago

To test our new densimeter on natural samples, we collected Raman spectra on the bubbles of nine melt inclusions (S4) hosted in olivine from a prehistoric (10–14th Century) eruption of Fogo (Monte Cassanga, Galinheiros). Most of these inclusions (25(1,2), 29, 31, 32, 36) had two-phase bubbles with both Liquid and Vapor CO<sub>2</sub> visible at room temperature (particularly notable in S4, #31 and #29). The Cape Verde Archipelago (CVA) is located ~500 km off the west coast of Africa. Nine islands of the CVA are inhabited, with a population of ~450,000, of which ~35,900 live on the island of Fogo ([Ramalho, 2011](#)). Volcanic activity in the CVA started ~18 Ma ago. The only island with known historical activity is Fogo with its highly active volcano, Pico do Fogo, which erupted from 1951 to 1995 and began a new eruptive cycle in 2014 ([Mitchell et al., 1983](#); [Ramalho, 2011](#)). Pico do Fogo is one of the most active volcanoes in human history, with ~30 eruptions since its discovery in the 15th century. Highly explosive eruptions seemingly occur every ~3 kyr at Fogo ([Eisele et al., 2015](#)) yet there is no published pre-eruptive volatile data available, and a future event of such intensity would pose a significant threat to the Cape Verdean population and trans-Atlantic air traffic.

We followed the same procedures used for the FDCA for these melt inclusions. MI were heated to 37 °C using a rectangular Peltier stage with a center hole (TE technology CH-119-1.4-1.5) mounted using a silicon heat pad on an aluminum heat sink with a drilled-in center hole and connected to a DC power supply. The temperature of the ceramic plate (thermal conductivity of ~1 Wm<sup>-1</sup> K<sup>-1</sup>) was monitored in real-time using a thermocouple type K connected to a laptop computer through a USB adapter until the temperature reached a plateau at 37 °C (usually after ~15 min). The sample, mounted on a square or round

glass slide (thermal conductivity of ~1–2 Wm<sup>-1</sup> K<sup>-1</sup>) using Crystal Bond, was placed on the center of the stage, and left to equilibrate for at least 15 min while constantly monitoring the temperature. Because the thermal conductivity of the ceramic plate, glass slide and Fo-rich olivine crystal are all very similar (same order of magnitude and close to 1), we consider that it is a reasonable assumption that the thermal equilibration time for the ceramic plate should be more than enough to thermally equilibrate the sample as well. Spectra were then collected with a 50× objective and 15 mW laser power. We collected Ne spectra in between each analysis and also collected spectra of fused-silica capillary tubes (FSC) several times during the session to control the accuracy of our measurements. Mean FSC densities (for three FSC between 0.01 and 0.1 g/mL) showed accuracy better than 5% except for the lowest density 0.01 g/mL FSC (accuracy 13%) for which larger uncertainties are expected ([Fig. 5](#)). The full dataset can be found in the supplementary materials (S1) and is plotted in [Fig. 12a](#). To better compare density estimates from densimeters calibrated on other instruments, densities calculated from other densimeters were shifted to our densimeter using a simple linear regression of the high and low-density FDCA data as CO<sub>2</sub> standards so that the estimates from each densimeter are comparable.

Melt inclusion bubbles analyzed spanned densities from ~0.15 to ~0.55 g/mL and bubble CO<sub>2</sub> contents for three inclusions were calculated through mass balance, assuming a density of 2.8 g/mL for the basaltic glass. The highest densities measured corresponded to the bubbles observed with both L + V, while the lowest densities were measured in samples for which a single vapor phase was observed.

Volumes for the melt inclusions were determined using image analysis for the x-y cross sections and an average of x-y axes as an estimate of the depth z. The depth z was also measured using optical microscopy for comparison. To determine z by the optical method, we vertically calibrated our microscope using a micrometer and estimated the z-axis by focusing on the MI from top to bottom several times. The measurement of the z-axis using either of these methods (most commonly used in laboratories worldwide) can be the most significant source of error due to the irregular nature of MI (20% or more depending on size and shape; [Hanyu et al., 2020](#)). Recently, methods such as High-Resolution X-Ray Computed Tomography have been demonstrated a capacity to measure volumes with an accuracy better than 2% for MI and 9% for bubbles ([Hanyu et al., 2020](#)). It should be noted that ~20% is a significant amount of uncertainty for melt inclusion volumes and that better measurements are required if the goal is to obtain geochemically, petrologically and volcanologically significant data. However, further discussion on the uncertainty in melt inclusion volume measurements is beyond the scope of our study. Given the results from [Hanyu et al. \(2020\)](#) as well as some of our own unpublished results, we consider that the error associated with these measurements is at most 20% for the most irregular MI. We fit an ellipse to the melt inclusion cross-sectional photograph using least squares minimizations in the freeware image-processing software FIJI ([Schindelin et al., 2012](#)). We calculated melt inclusion volumes as idealized ellipsoids, and bubble volumes assuming spheres for which the radial axis was measured by fitting a sphere following a similar procedure as was described for the ellipses. We consider these assumptions to be reasonable given that the purpose of these data is only to compare estimates of density given by different CO<sub>2</sub> standard corrected densimeters. It is extremely important to note that these estimates of CO<sub>2</sub> contents are in no way intended to provide interpretation of the Fogo eruption and should not be used to this end. Rather, they simply illustrate the use of our new densimeter.

Even after shifting densimeters using CO<sub>2</sub> standards, CO<sub>2</sub> densities for these melt inclusion bubbles could be overestimated by up to ~0.045 g/mL using densimeters from the literature compared to the equations calibrated here. The difference in density compared to our densimeter in the low-density region (<0.2 g/mL) is lower than 0.02 g/mL for all densimeters and lower than 0.01 g/mL for all except [Yamamoto and Kagi \(2006, 3<sup>rd</sup> degree polynomial\)](#), [Rosso and Bodnar \(1995\)](#) and [Song et al. \(2009\)](#). However, in the most sensitive critical region, the



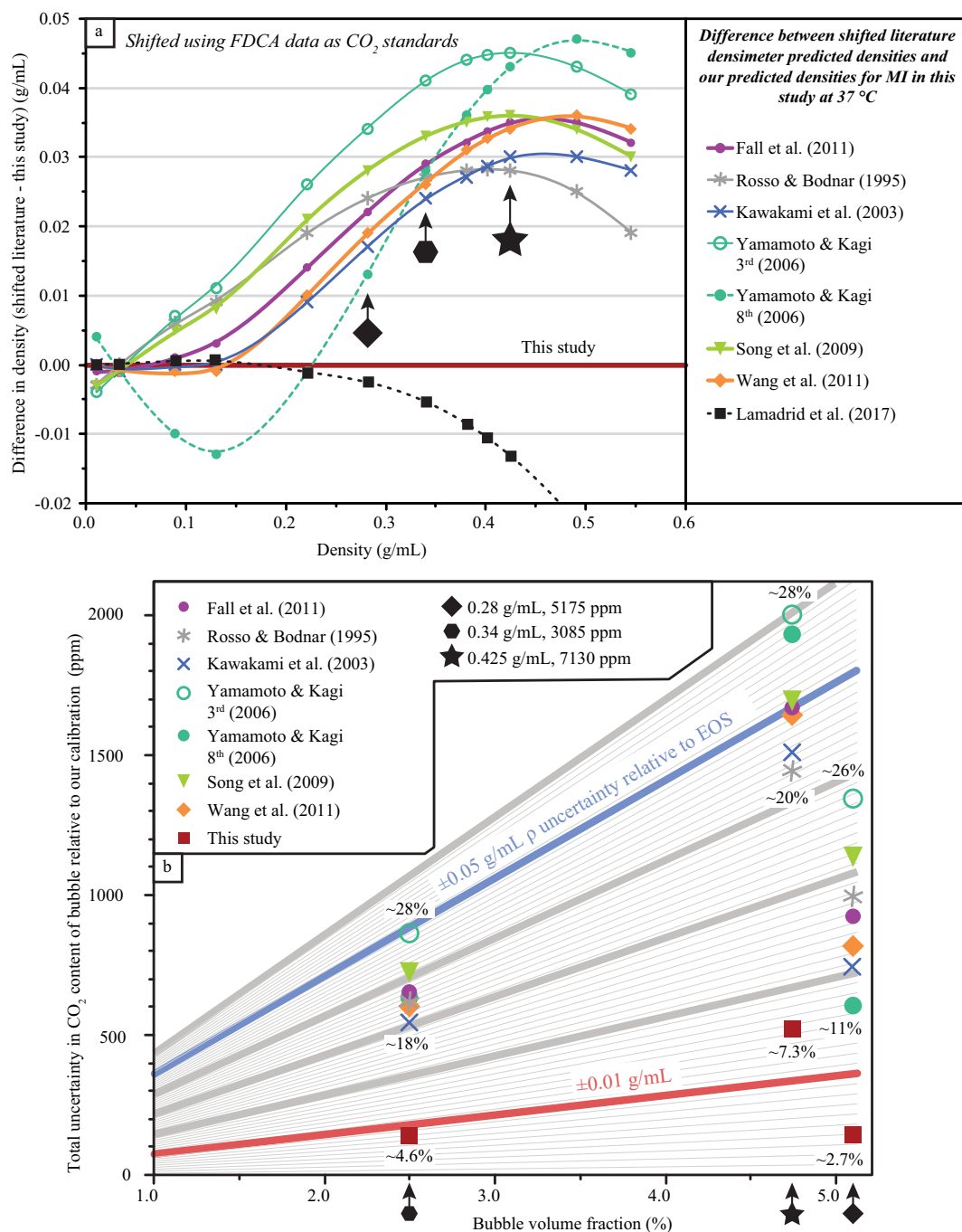


**Fig. 12.** Comparison of results from densimeters using melt inclusion data. a) Differences in the density of 8 melt inclusion bubbles from Fogo calculated by published densimeters shifted relative to our new densimeter. The density estimates from literature densimeters are shifted to our calibration data using a simple 3-point linear regression points in the 37 °C dataset and differences are calculated. The mid-density region is of particular interest here (~0.2–0.7 g/mL) b) Total uncertainty in ppm CO<sub>2</sub> content of melt inclusion bubbles calculated for different uncertainties in density relative to the EOS and as a function of the volume% occupied by the bubble. The relative uncertainty in density from literature densimeters for our unknown data is estimated considering the differences relative to our new densimeter from panel a) in addition to the propagated total absolute uncertainty of our densimeter relative to the EOS at each density (Fig. 6). We want to stress that this is not an assessment of the true accuracy of other densimeters but rather represents how far off our own measurements at mid-density (~0.3–0.5 g/mL) would be from an accepted density if we used a literature densimeter shifted using CO<sub>2</sub> standards instead of our own. Specific total uncertainty percent are calculated for 3 MI bubbles and different densimeters.

differences are at least 0.03 g/mL and up to nearly 0.05 g/mL. These are very notable density differences; our 37 °C densimeter-predicted densities are at worst ~0.011 g/mL different from EOS-calculated values in the sensitive critical region. This suggests that the existing densimeters, even after an adjustment using CO<sub>2</sub> standards, do not accurately estimate the CO<sub>2</sub> density of these samples measured on our instrument.

In Fig. 12b we estimate how this total uncertainty translates to the

uncertainty on the CO<sub>2</sub> contents of the bubbles depending on the relative size of the bubble compared to the inclusion. This is particularly significant for mid-densities and high-volume fraction bubbles (ratio of volume of the bubble to volume of the inclusion) where total errors can amount to 1000–2000 ppm CO<sub>2</sub> depending on the densimeter. Additionally, we calculated the total percent error corresponding to each estimate; for example, 500 ppm CO<sub>2</sub> error is 6.5% total error for a 0.425

g/mL and 5% volume fraction bubble but represents ~13% error if the bubble was instead 2.5% volume fraction. Total percent uncertainty calculated for our densimeter are always below 5% except for inclusions with densities in the most sensitive part of the critical region (~7.3% for a 0.425 g/mL bubble), while relative percent uncertainty for other densimeters are always above 10% and up to 28% in the worst-case scenario. This relative percent uncertainty is not intended as an estimate of the real uncertainty in each densimeter, which can only be measured when comparing each densimeter with its own data (e.g., Fig. 10). Instead, it is meant to illustrate the effect of using a densimeter not calibrated for the instrument used to analyze unknowns. This exercise demonstrates that densimeters must be calibrated for individual Raman instruments and settings of those instruments, as previously discussed by Lamadrid et al. (2017) for low density data (<0.2 g/mL). However, we also find that the calibration of densimeters in the critical region must be carefully considered to reduce the error on CO<sub>2</sub> estimates for fluid and melt inclusions with mid-densities as much as possible.

## 6. Conclusions

We presented a redesigned FDCA for calibration of CO<sub>2</sub> densimeters for Raman spectroscopy. The FDCA measures both temperature and pressure inside the CO<sub>2</sub> chamber, yielding excellent accuracy of CO<sub>2</sub> densities. We proposed five highly precise new calibration equations for different temperatures and CO<sub>2</sub> density ranges. From this work, we make the following recommendations regarding calibration of Raman spectrometers for CO<sub>2</sub> densities:

- Ideally, as also suggested by Lamadrid et al. (2017), an FDCA should be built for the Raman instrument used to analyze unknowns which should always be corrected for non-linearity of the Raman shift axis. If construction of an FDCA is not viable, unknown sample data should be shifted using two or more known density standards when calculating the density of CO<sub>2</sub> using any densimeter and the standards should span the range of the CO<sub>2</sub> densities of the unknowns.
- For any FDCA apparatus, high accuracy thermometers ( $\pm 0.05$  °C) calibrated for the temperatures of the analyses should be placed inside the apparatus to measure the temperature of the fluid directly. This is because the differences between densimeters are largest for mid-densities of CO<sub>2</sub>, which might be partly explained by uncertainties in the temperature measurements.
- Temperature should be held constant during Raman measurements of the FDCA at both room temperature and supercritical temperature to ensure maximum stability of the calibration. The use of a thermoelectric plate is highly recommended for this purpose.
- To reduce uncertainty from densimeter equations, separate calibrations should be completed for measurements at different temperatures.

## Declaration of Competing Interest

The authors declare that they have no known competing financial interests or personal relationships that could have appeared to influence the work reported in this paper.

## Acknowledgments

We thank Phil Carubia at the Cornell Center for Materials Research for his assistance in the early stages of the FDCA construction and training on the Raman instrument. We thank Jay Thomas (Syracuse University), Kurt Roggensack (Arizona State University), and Kurt Leinenweber (Arizona State University) for discussions regarding FDCA designs. We also thank Ricardo Ramalho (University of Cardiff) for

providing the Pico do Fogo sample, Emmanuel Soignard (Arizona State University) for the MATLAB code used to peak-fit the Raman data. We thank the reviewers for providing a wealth of constructive suggestions that aided in substantially improving the quality of this manuscript. This project was supported in part by NSF awards OCE 1756349 and EAR 1826673 to EG. This work made use of the Cornell Center for Materials Research Shared Facilities which are supported through the NSF MRSEC program (DMR-1719875)

## Appendix A. Supplementary data

Supplementary data to this article can be found online at <https://doi.org/10.1016/j.chemgeo.2021.120522>.

## References

- Ague, J.J., 2017. Element mobility during regional metamorphism in crustal and subduction zone environments with a focus on the rare earth elements (REE). *Am. Mineral.* 102, 1796–1821. <https://doi.org/10.2138/am-2017-6130>.
- Allison, C.M., Roggensack, K., Clarke, A.B., 2021. Highly explosive basaltic eruptions driven by CO<sub>2</sub> exsolution. *Nat. Commun.* 12, 1–10. <https://doi.org/10.1038/s41467-020-20354-2>.
- Andersen, T., Neumann, E.-R., 2001. Fluid inclusions in mantle xenoliths. *Lithos* 55, 301–320. [https://doi.org/10.1016/S0024-4937\(00\)00049-9](https://doi.org/10.1016/S0024-4937(00)00049-9).
- Aster, E.M., Wallace, P.J., Moore, L.R., Watkins, J., Gazel, E., Bodnar, R.J., 2016. Reconstructing CO<sub>2</sub> concentrations in basaltic melt inclusions using Raman analysis of vapor bubbles. *J. Volcanol. Geotherm. Res.* 323, 148–162. <https://doi.org/10.1016/j.jvolgeores.2016.04.028>.
- Baker, T., 2002. Emplacement depth and carbon-dioxide rich fluid inclusions in intrusion-related gold deposits. *Econ. Geol.* 97, 1111–1117. <https://doi.org/10.2113/gsecongeo.97.5.1111>.
- Chang, Y.-Y., Hsieh, W.-P., Tan, E., Chen, J., 2017. Hydration-reduced lattice thermal conductivity of olivine in Earth's upper mantle. *PNAS* 114, 4078–4081. <https://doi.org/10.1073/pnas.1616216114>.
- Dasgupta, R., Hirschmann, M.M., 2010. The deep carbon cycle and melting in Earth's interior. *Earth Planet. Sci. Lett.* 298, 1.
- Dasgupta, R., Hirschmann, M.M., Withers, A.C., 2004. Deep global cycling of carbon constrained by the solidus of anhydrous, carbonated eclogite under upper mantle conditions. *Earth Planet. Sci. Lett.* 227, 73–85. <https://doi.org/10.1016/j.epsl.2004.08.004>.
- Diamond, L.W., 2003. Introduction to gas-bearing, aqueous fluid inclusions. *Fluid Incl. Anal. Interpret.* 32, 101–158.
- Dickinson, R.G., Dillon, R.T., Rasetti, F., 1929. Raman spectra of polyatomic gases. *Phys. Rev.* 34, 582–589. <https://doi.org/10.1103/PhysRev.34.582>.
- Duschkew, W., Kleinrahm, R., Wagner, W., 1990. Measurement and correlation of the (pressure, density, temperature) relation of carbon dioxide II. Saturated-liquid and saturated-vapour densities and the vapour pressure along the entire coexistence curve. *J. Chem. Thermodyn.* 22, 841–864. [https://doi.org/10.1016/0021-9614\(90\)90173-N](https://doi.org/10.1016/0021-9614(90)90173-N).
- Eisele, S., Reißig, S., Freundt, A., Kutterolf, S., Nürnberg, D., Wang, K.L., Kwasnitschka, T., 2015. Pleistocene to Holocene offshore tephrostratigraphy of highly explosive eruptions from the southwestern Cape Verde Archipelago. *Mar. Geol.* 369, 233–250. <https://doi.org/10.1016/j.margeo.2015.09.006>.
- Esposito, R., Klebesz, R., Bartoli, O., Klyukin, Y., Moncada, D., Doherty, A., Bodnar, R., 2012. Application of the Linkam TS1400XY heating stage to melt inclusion studies. *Open Geosci.* 4, 208–218.
- Fall, A., Tattitch, B., Bodnar, R.J., 2011. Combined microthermometric and Raman spectroscopic technique to determine the salinity of H<sub>2</sub>O–CO<sub>2</sub>–NaCl fluid inclusions based on clathrate melting. *Geochim. Cosmochim. Acta* 75, 951–964. <https://doi.org/10.1016/j.gca.2010.11.021>.
- Fan, H.-R., Hu, F.-F., Wang, K.-Y., Xie, Y.-H., 2005. Aqueous-carbonic-REE fluids in the giant Bayan Obo deposit, China: Implications for REE mineralization. In: Mao, J., Bierlein, F.P. (Eds.), *Mineral Deposit Research: Meeting the Global Challenge*. Springer, Berlin Heidelberg, Berlin, Heidelberg, pp. 945–948.
- Fermi, E., 1931. Über den Raman-Effekt des Kohlendioxyds. *Z. Für Phys.* 71, 250. <https://doi.org/10.1007/bf01341712>.
- Fukura, S., Mizukami, T., Odake, S., Kagi, H., 2006. Factors determining the stability, resolution, and precision of a conventional Raman spectrometer. *Appl. Spectrosc.* 60, 946–950. <https://doi.org/10.1366/000370206778062165>.
- Garrabos, Y., Tufeu, R., Le Neindre, B., Zalczer, G., Beysens, D., 1980. Rayleigh and Raman scattering near the critical point of carbon dioxide. *J. Chem. Phys.* 72, 4637–4651.
- Garrabos, Y., Chandrasekharan, V., Echargui, M.A., Marsault-Herail, F., 1989a. Density effect on the Raman Fermi resonance in the fluid phases of CO<sub>2</sub>. *Chem. Phys. Lett.* 160, 250–256. [https://doi.org/10.1016/0009-2614\(89\)87591-8](https://doi.org/10.1016/0009-2614(89)87591-8).
- Garrabos, Y., Echargui, M.A., Marsault-Herail, F., 1989b. Comparison between the density effects on the levels of the Raman spectra of the Fermi resonance doublet of the 12C16O<sub>2</sub> and 13C16O<sub>2</sub> molecules. *J. Chem. Phys.* 91, 5869–5881.
- Gaufres, R., Huguet, P., Arab, Y., 1995. Method for the determination of spectral shifts in Raman spectroscopy. *J. Raman Spectrosc.* 26, 243–253. <https://doi.org/10.1002/jrs.1250260307>.

- Gordon, H.R., McCubbin, T.K., 1966. The 2.8-micron bands of CO<sub>2</sub>. *J. Mol. Spectrosc.* 19, 137–154. [https://doi.org/10.1016/0022-2852\(66\)90237-2](https://doi.org/10.1016/0022-2852(66)90237-2).
- Groves, D.L., Goldfarb, R.J., Robert, F., Hart, C.J.R., 2003. Gold deposits in metamorphic belts: overview of current understanding, outstanding problems, future research, and exploration significance. *Econ. Geol.* 98, 1–29. <https://doi.org/10.2113/gsecongeo.98.1.1>.
- Hanyu, T., Yamamoto, J., Kimoto, K., Shimizu, K., Ushikubo, T., 2020. Determination of total CO<sub>2</sub> in melt inclusions with shrinkage bubbles. *Chem. Geol.* 557, 119855. <https://doi.org/10.1016/j.chemgeo.2020.119855>.
- Hollister, L.S., 1981. Information intrinsically available from fluid inclusions. *Min. Assoc. Can. Short Course Hand* 6, 1–12.
- Howard-Lock, H.E., Stoicheff, B.P., 1971. Raman intensity measurements of the Fermi diad  $\nu_1$ ,  $2\nu_2$  in 12CO<sub>2</sub> and 13CO<sub>2</sub>. *J. Mol. Spectrosc.* 37, 321–326. [https://doi.org/10.1016/0022-2852\(71\)90302-X](https://doi.org/10.1016/0022-2852(71)90302-X).
- Kawakami, Y., Yamamoto, J., Kagi, H., 2003. Micro-Raman densimeter for CO<sub>2</sub> inclusions in mantle-derived minerals. *Appl. Spectrosc.* 57, 1333–1339. <https://doi.org/10.1016/j.chemgeo.2016.12.034>.
- Lamadrid, H.M., Moore, L.R., Moncada, D., Rimstidt, J.D., Burruss, R.C., Bodnar, R.J., 2017. Reassessment of the Raman CO<sub>2</sub> densimeter. *Chem. Geol.* 450, 210–222. <https://doi.org/10.1016/j.chemgeo.2016.12.034>.
- Lin, F., Bodnar, R.J., Becker, S.P., 2007. Experimental determination of the Raman CH<sub>4</sub> symmetric stretching ( $\nu_1$ ) band position from 1–650bar and 0.3–22°C: application to fluid inclusion studies. *Geochim. Cosmochim. Acta* 71, 3746–3756. <https://doi.org/10.1016/j.gca.2007.05.016>.
- McCreery, R.L., 2005. *Raman Spectroscopy for Chemical Analysis*. John Wiley & Sons.
- Mestari, A., Gauffrès, R., Hugué, P., 1997. Behaviour of the calibration of a Raman spectrometer with temperature changes. *J. Raman Spectrosc.* 28, 785–789.
- Mitchell, J.G., Le Bas, M.J., Zielonka, J., Furnes, H., 1983. On dating the magmatism of Maio, Cape Verde Islands. *Earth Planet. Sci. Lett.* 64, 61–76. [https://doi.org/10.1016/0012-821X\(83\)90053-5](https://doi.org/10.1016/0012-821X(83)90053-5).
- Moore, L.R., Gazel, E., Tuohy, R., Lloyd, A.S., Esposito, R., Steele-MacInnis, M., Hauri, E. H., Wallace, P.J., Plank, T., Bodnar, R.J., 2015. Bubbles matter: an assessment of the contribution of vapor bubbles to melt inclusion volatile budgets. *Am. Mineral.* 100, 806–823. <https://doi.org/10.2138/am-2015-5036>.
- Ramalho, R.A.S., 2011. *Building the Cape Verde Islands*. Springer Science & Business Media.
- Roedder, E., 1965. Liquid CO<sub>2</sub> inclusions in olivine-bearing nodules and phenocrysts from basalts. *Am. Mineral. J. Earth Planet. Mater.* 50, 1746–1782.
- Roedder, E., 1979. Origin and significance of magmatic inclusions. *Bull. Mineral.* 102, 487–510. <https://doi.org/10.3406/bulmi.1979.7299>.
- Roedder, E., 1984. Fluid inclusions. In: *Reviews in Mineralogy*, vol. 12. Mineral. Soc. Am, Wash. DC.
- Roggensack, K., Hervig, R.L., McKnight, S.B., Williams, S.N., 1997. Explosive basaltic volcanism from Cerro Negro volcano: influence of volatiles on eruptive style. *Science* 277, 1639–1642. <https://doi.org/10.1126/science.277.5332.1639>.
- Rosso, K.M., Bodnar, R.J., 1995. Microthermometric and Raman spectroscopic detection limits of CO<sub>2</sub> in fluid inclusions and the Raman spectroscopic characterization of CO<sub>2</sub>. *Geochim. Cosmochim. Acta* 59, 3961–3975. [https://doi.org/10.1016/0016-7037\(95\)94441-H](https://doi.org/10.1016/0016-7037(95)94441-H).
- Schindelin, J., Arganda-Carreras, I., Frise, E., Kaynig, V., Longair, M., Pietzsch, T., Preibisch, S., Rueden, C., Saalfeld, S., Schmid, B., Tinevez, J.-Y., White, D.J., Hartenstein, V., Eliceiri, K., Tomancak, P., Cardona, A., 2012. Fiji: an open-source platform for biological-image analysis. *Nat Methods* 9, 676–682. <https://doi.org/10.1038/nmeth.2019>.
- Song, Y., Chou, I., Hu, W., Robert, B., Lu, W., 2009. CO<sub>2</sub> density-Raman shift relation derived from synthetic inclusions in fused silica capillaries and its application. *Acta Geol. Sin. Ed.* 83, 932–938.
- Span, R., Wagner, W., 1996. A new equation of state for carbon dioxide covering the fluid region from the triple-point temperature to 1100 K at pressures up to 800 MPa. *J. Phys. Chem. Ref. Data* 25, 1509–1596.
- Steele-Macinnis, M., Esposito, R., Bodnar, R.J., 2011. Thermodynamic model for the effect of post-entrapment crystallization on the H<sub>2</sub>O–CO<sub>2</sub> Systematics of vapor-saturated, silicate melt inclusions. *J. Petrol.* 52, 2461–2482. <https://doi.org/10.1093/petrology/egr052>.
- Sterner, S.M., Pitzer, K.S., 1994. An equation of state for carbon dioxide valid from zero to extreme pressures. *Contrib. Mineral. Petrol.* 117, 362–374.
- Wang, X., Chou, I.-M., Hu, W., Burruss, R.C., Sun, Q., Song, Y., 2011. Raman spectroscopic measurements of CO<sub>2</sub> density: experimental calibration with high-pressure optical cell (HPOC) and fused silica capillary capsule (FSCC) with application to fluid inclusion observations. *Geochim. Cosmochim. Acta* 75, 4080–4093. <https://doi.org/10.1016/j.gca.2011.04.028>.
- Wieser, P.E., Lamadrid, H., MacLennan, J., Edmonds, M., Matthews, S., Iacovino, K., Jenner, F.E., Gansecki, C., Trusdell, F., Lee, R.L., Ilyinskaya, E., 2021. Reconstructing magma storage depths for the 2018 Kīlauea eruption from melt inclusion CO<sub>2</sub> contents: the importance of vapor bubbles. *Geochim. Geophys. Geosyst.* 22 <https://doi.org/10.1029/2020GC009364> e2020GC009364.
- Wojdyr, M., 2010. Fityk: a general-purpose peak fitting program. *J. Appl. Cryst.* 43, 1126–1128. <https://doi.org/10.1107/S0021889810030499>.
- Xie, Y., Hou, Z., Yin, S., Dominy, S.C., Xu, J., Tian, S., Xu, W., 2009. Continuous carbonatitic melt–fluid evolution of a REE mineralization system: evidence from inclusions in the Maoniuping REE Deposit, Western Sichuan, China. *Ore Geol. Rev.* 36, 90–105.
- Xiong, Z., Zhang, B., 2019. Thermal transport properties of Olivine, Wadsleyite, and Ringwoodite—a review. *Minerals* 9, 519. <https://doi.org/10.3390/min9090519>.
- Yamamoto, J., Kagi, H., 2006. Extended micro-Raman densimeter for CO<sub>2</sub> applicable to mantle-originated fluid inclusions. *Chem. Lett.* 35, 610–611.